

Benchmark Study Matrix for Microreactor Geometries Relevant to Multiple Developers

M3CT-24PN1307031

September 2024

Isabella van Rooyen
James Fitzpatrick
Nathan Barrett
CJ Taylor Mason
Subhashish Meher
Daniel Yoon
Robert Montgomery
Chris Hutchinson
Mohan Nartu

DISCLAIMER

This report was prepared as an account of work sponsored by an agency of the United States Government. Neither the United States Government nor any agency thereof, nor Battelle Memorial Institute, nor any of their employees, makes **any warranty, express or implied, or assumes any legal liability or responsibility for the accuracy, completeness, or usefulness of any information, apparatus, product, or process disclosed, or represents that its use would not infringe privately owned rights.** Reference herein to any specific commercial product, process, or service by trade name, trademark, manufacturer, or otherwise does not necessarily constitute or imply its endorsement, recommendation, or favoring by the United States Government or any agency thereof, or Battelle Memorial Institute. The views and opinions of authors expressed herein do not necessarily state or reflect those of the United States Government or any agency thereof.

PACIFIC NORTHWEST NATIONAL LABORATORY
operated by
BATTELLE
for the
UNITED STATES DEPARTMENT OF ENERGY
under Contract DE-AC05-76RL01830

Printed in the United States of America

Available to DOE and DOE contractors from
the Office of Scientific and Technical Information,
P.O. Box 62, Oak Ridge, TN 37831-0062

www.osti.gov
ph: (865) 576-8401
fax: (865) 576-5728
email: reports@osti.gov

Available to the public from the National Technical Information Service
5301 Shawnee Rd., Alexandria, VA 22312
ph: (800) 553-NTIS (6847)
or (703) 605-6000
email: info@ntis.gov
Online ordering: <http://www.ntis.gov>

Benchmark Study Matrix for Microreactor Geometries Relevant to Multiple Developers

M3CT-24PN1307031

September 2024

Isabella van Rooyen
James Fitzpatrick
Nathan Barrett
CJ Taylor Mason
Subhashish Meher
Daniel Yoon
Robert Montgomery
Chris Hutchinson
Mohan Nartu

Prepared for
the U.S. Department of Energy
under Contract DE-AC05-76RL01830

Pacific Northwest National Laboratory
Richland, Washington 99354

Summary

A benchmark study was developed that include design, development, manufacturing, and performance measurement of agnostic reactor relevant geometries to support industry's adoption of advanced manufacturing in a variety of structures. A matrix of five microreactor component geometries, specifically based on the recent feasibility study on a Marvel microreactor liner, was developed and the Pacific Northwest National Laboratory team initiated one material/process combination, namely 316H using laser powder directed energy deposition (DED). Although the benchmark starts initially with simplistic cubical and cylindrical forms, it builds up to a mock-up of a non-proprietary design that can demonstrate a variety of features potentially useful for presenting knowledge to specific designers of microreactors and for the matter also for other reactor type designers. The initial cubical and cylindrical forms are initial steps to obtain surface features and dimensional responses to the identified process parameters to be used in the non-proprietary design mockup.

The powder DED technique has been identified as the technique for the fiscal year 2024 benchmark study due to multiple reasons, namely:

- leverage cylindrical sample pieces manufactured during the development stages of the full-scale DED 316L stainless-steel (SS) liner,
- increased industry interest
- to minimize overlap with the large investment in laser powder bed fusion project scope of the Advanced Materials and Manufacturing Technology (AMMT) program
- provide information that will decrease the gap in knowledge and data for codes and standards
- interest from the international Generation IV International Forum (GIF) community
- the potential for complex parts with unique options to minimize weldments
- prevent overlap with the GIF Material board research projects that is currently been finalized.

By performing the benchmark study, the AMMT program will provide nuclear energy stakeholders another manufacturing option and knowledge to apply for accelerated readiness for new or replacement designs, therefore accelerating demonstration.

This project proposes using an expanded pipe that leads into an elbow. Not only is this component extremely difficult and costly to manufacture through traditional methods, but it can also reduce the space needed for traditional transition areas. This design allows for a smooth transition from a larger pipe to a smaller pipe at the location of a 90° bend and has potential to increase fluid flow and reduce turbulence. Thus, the expanded elbow pipe is an excellent candidate for demonstrating the ability to use DED for manufacturing of microreactor components.

Although only limited characterization was completed, the main findings are described below:

1. 316H SS cubical samples: A 316H SS powder DED literature survey and a parameter confirmation study on 16 cubical samples were performed for power levels of 400–700 W and scan speeds ranged from 600–900 mm/min. It was found that the quality (based on porosity content) is independent of scan speed for a laser power of 700 W. However, at lower laser

power, it seems that the lower scan speed yields larger porosity levels and larger in size defects. These parameters are being used for the printing of the cylindrical samples currently in process.

2. 316L SS cylindrical sample: The evaluation on the cylinder from 316L SS yield good agreement between the wall thickness measurements obtained from the destructive optical technique and the non-destructive evaluation method. The impact of the surface roughness on both destructive and non-destructive measurements is observed and is necessary to be explored further for full application and resolution. Based on these measurements, the surface roughness is on the order of 0.1–0.2 mm. Although metallurgical examination of the 316L SS cylinder sample is not completed, it is noted that the cellular structure is similar between samples from the top and bottom. Segregation is noted in these cellular cells as the cell walls are lean in iron and slightly enriched in chromium. It is recommended that this to be compared with other studies.

The finite element modeling and analysis effort that has been performed to understand the temperature field, residual stresses, and deformation present at the conclusion of the DED build process for a 316L SS cylinder. The assumed build parameters were a deposition speed of 2 cm/s, a material melt temperature of 1,375 °C, a bottom surface baseplate temperature held at 80°C, 2 hours of cooldown time, an ambient environmental temperature, and film coefficient of 25°C and $10 \frac{W}{m^2K}$, respectively. Two deposition path styles were described and modeled: 1) circumferential style and 2) raster style. At this time, these build parameters are assumed, because the actual build parameters used in the fabrication of the cylinder were not available at the time of publishing the work. The finite element model was used in both a thermal and structural analysis, with the thermal analysis performed before the structural analysis. The thermal analysis provided the temperature field of the component during the build process and the 2-hour cooldown after the build. The structural analysis used the time-history temperature field data to determine the residual stresses and deformations in the cylinder during the build, cooldown period, and baseplate removal.

1. Results from the finite element analyses were presented for both deposition paths. The differences between the temperature fields, residual stresses, and cylinder deformations in each are presented and described. Notably, this process of using the finite element analysis to determine the resulting temperatures, stresses, and deformations can be used in future analyses to determine optimal build paths during future DED fabrication efforts.
2. The next steps for this work will be to implement build parameters that accurately represent the experimentally fabricated cylinder. Once these parameters have been obtained, a representative finite element analysis study can be conducted. The 316L SS cylinder that has been fabricated using DED could be examined to determine the residual stresses present in the physical part. These stresses then could be compared to the finite element analysis results to determine the accuracy of the model and for further refinement as needed. Additionally, future modeling efforts could include the modeling of alternate materials such as a 316H SS cylinder with the same geometry presented in this work.
3. Additional work that should be performed for this modeling effort is a mesh refinement study that determines the optimal mesh density for the cylinder. This includes determining the adequate number of layers vertically along the cylinder axis and radially through the cylinder wall thickness that provide enough detail to assure accuracy.
4. Finally, future work exploring finite element modeling of potential DED components to be used in microreactors, such as expanded elbow pipes, expanded straight pipes, two-axis pipes, flanged elbows without expansion, heat exchangers, pumps, and valves, should be performed.

In conclusion, the geometry benchmark matrix with associated characterization matrix form would be a good basis for continuation for the 316H SS/DED combination, which can be expanded to a 316H SS/laser powder bed fusion combination to evaluate the different effects if these two processes are used and to leverage the parameter optimization work performed under other AMMT program projects.

Acknowledgments

The research presented here was supported by the Advanced Materials and Manufacturing Technology program of the U.S. Department of Energy (DOE) Office of Nuclear Energy. Pacific Northwest National Laboratory is a multi-program national laboratory operated for the DOE by Battelle Memorial Institute under Contract No. DE-AC05-76RL01830. Professor Xiao Lou from Purdue University is acknowledged for printing of the 316H stainless-steel (SS) directed energy deposition (DED) component series, and RPMi is acknowledged for the DED printing of the 316L SS small cylinder as well as the full-scale 316L SS Marvel liner. Dr. Stu Malloy is thanked for the coordination of the 316L SS liner and cylinder DED printing. Cary Counts is thanked for his editorial review of this report. Dr Carolynne Burns is thanked for his technical review of the report and its contents.

Acronyms and Abbreviations

AMMT	Advanced Materials and Manufacturing Technologies
AM	Advanced Manufacturing
MARVEL	Microreactor Application Research, Validation and Evaluation Project
DED	directed energy deposition
DIC	Digital image correlation
EBSD	Electron backscattering diffraction
EDS	Energy-Dispersive Spectroscopy
FEA	finite element analysis
FFT	Fast Fourier Transform
FY	fiscal year
INL	Idaho National Laboratory
ID	inner diameter
KAM	kernel average misorientation
LPBF	laser powder bed fusion
MSR	molten-salt reactors
NDE	nondestructive evaluation
OD	outer diameter
PNNL	Pacific Northwest National Laboratory
SEM	scanning electron microscopy
SLM	selective laser melting
SS	stainless steel

Contents

Summary	ii
Acknowledgments.....	v
Acronyms and Abbreviations.....	vi
1.0 Introduction	1
1.1 Background.....	1
1.2 Scope	2
2.0 Benchmark Study Development	3
2.1 Identification of the AM Technique for the Benchmark Study	3
2.2 Identification and Motivation on the Material Type to be used for the Benchmark Study.....	5
2.3 Identification and Motivation of the Geometries to be Used for This Benchmark Study.....	6
2.4 Evaluation of Advanced Reactor Geometries and Design of Agnostic Non-Proprietary Mock-Up Component for the Benchmark Study	7
2.5 Identification and Motivation of the Characterization or Performance Testing to be used for this Benchmark Study	11
3.0 316H Stainless Steel Survey and Cube Preliminary Evaluation	12
3.1 316L and 316H Powder DED	12
3.2 Residual Stresses: Origin, Mechanism, Process Parameters that Affect Lower or Higher Residual Stress Output	14
3.3 Methods for Determining Residual Stresses	17
3.4 316H Stainless Steel Cube Samples: Preliminary Results	21
4.0 Preliminary Results on 316L SS Cylindrical Samples	24
4.1 Experimentally Fabricated 316L Cylinder	24
4.2 Finite Element Modeling for DED Fabrication Processes	25
4.2.1 Transient Thermal Model	25
4.2.2 Static Structural Model.....	28
4.2.3 Finite Element Model Results.....	30
4.3 SS316L SS Cylinder: Evaluation and Characterization	37
4.3.1 NDE Summary.....	37
4.3.2 Metallurgical Analysis	42
5.0 Full Scale 316L SS Microreactor Heat Exchange Liner: Preliminary Results	45
6.0 Summary and Future Work.....	47
7.0 References.....	50

Figures

Figure 1.	Industry interest in AM techniques based on the GIF-AMME WG 2023 industry survey (Van Rooyen, 2024)	4
Figure 2.	Dimensional application space for various AM processes as adapted from Gradl et. al., 2022	4
Figure 3.	Number of times a material was referenced by survey participants as a candidate for AM for nuclear application (Hartmann et.al., 2022)	5
Figure 4.	Dimensions of the benchmark samples identified in Table 1	7
Figure 5.	Example of guard vessel (Jackson, 2024).....	9
Figure 6.	Schematic of the internal heat exchangers within the MARVEL Microreactor (Laboratory, 2022).....	9
Figure 7.	Draft schematic of expanded elbow pipe (dimensions are in inches)	10
Figure 8.	Initial draft schematic of two-axis pipe.....	10
Figure 9.	Example graphic of flanged elbow pipe without expansion (MDC Precision, 2023)	10
Figure 10.	Example Schematic of Pump Impeller (Orye, 2021).....	10
Figure 11.	Example schematic of check valve (Khan, 2023)	11
Figure 12.	DED Optomec LENS machine study data on laser power and porosity.....	14
Figure 13.	Mechanisms of residual stress formation in MAM. Note. Reproduced from Chen, et. al., 2022. CC-BY.....	15
Figure 14.	Scanning strategy for MAM. (a)-(f) Scanning strategy in a single layer; (g) and (h) relationship between layers. Note. Reproduced from Chen, et. al., 2022. CC-BY.....	16
Figure 15.	Neutron diffraction schematic of a sample measurement setup. Note. Reproduced from Goel et. al., 2020. CC-BY	18
Figure 16.	X-ray diffraction schematic to determine residual stresses. Note. Reproduced from Huan et. al., 2020. CC-BY	18
Figure 17.	DIC results of the displacements W (a,c) and U (b,d) for the four points C0, C1, C2, C3. The plots (a,b) presents the average value for various drilling depths. The contours (c,d) as seen in VIC-3D, illustrate the displacement field for a drilling depth of 1.2 mm. Note. Reproduced from Polyzos et. al., 2023. CC-BY.....	19
Figure 18.	Measurements of residual stress by hole drilling (A), crack compliance method (B), and contour method (C). Note. Reproduced from Roehling et. al., 2019. CC-BY.....	20
Figure 19.	Schematic diagram showing the experimental set-up for EBSD observations. Note. Reproduced from by Wilkinson and Britton, 2012 CC-BY.....	21
Figure 20.	Sixteen individually DED fabricated cubes of 316H SS.	22
Figure 21.	Optical micrographs of the XZ cross sections of 316H SS samples produced at various laser power and scan speeds.....	22
Figure 22.	Effect of DED process parameters; laser power (W) at four different scan speeds (mm/min) on SS316H samples.....	23

Figure 23.	Effect of DED process parameters. Scan speed (mm/min) at four different laser powers (W) on 316H SS samples.....	23
Figure 24.	316L SS cylinder geometry	24
Figure 25.	316L SS cylinder finite element model geometry	26
Figure 26.	Deposition paths. Circumferential style (a) and raster style (b).....	27
Figure 27.	Layer-wise mean temperature (K). Circumferential style build (a) and raster style build (b)	30
Figure 28.	Part temperature (K) at completion of build (fabrication step 25). Circumferential style build (a) and raster style build (b).	30
Figure 29.	Layer-wise inner hoop stress (MPa). Circumferential style build (a) and raster style build (b).	31
Figure 30.	Layer-wise outer hoop stress (MPa). Circumferential style build (a) and raster style build (b)	32
Figure 31.	Layer-wise total hoop stress (MPa). Circumferential style build (a) and raster style build (b).	32
Figure 32.	Part hoop stress (MPa) at completion of build (fabrication step 25). Circumferential style build (a) and raster style build (b)	33
Figure 33.	Part hoop stress (MPa) at post-cooling, pre-baseplate removal. Circumferential style build (a) and raster style build (b)	33
Figure 34.	Part hoop stress (MPa) at post-cooling, post-baseplate removal. Circumferential style build (a) and raster style build (b)	33
Figure 35.	Post-cooling layer-wise inner hoop stress. Circumferential style build (a) and raster style build (b).....	34
Figure 36.	Post-cooling layer-wise outer hoop stress. Circumferential style build (a) and raster style build (b).....	35
Figure 37.	Post-cooling layer-wise total hoop stress. Circumferential style build (a) and raster style build (b).....	35
Figure 38.	Post-cooling comparative hoop stress.....	36
Figure 39.	Deformed shape magnified 6x, side profile view. Circumferential style build (a) and raster style build (b)	37
Figure 40.	Deformed shape magnified 6x, top view. Circumferential style build (a) and raster style build (b).....	37
Figure 41.	Scanner and transducer setup for NDE of the DED 316L component	39
Figure 42.	DED 316L SS component wall thickness contour map from the ultrasonic NDE measurements. Machined surface zones are indicated by text. Locations for wall thickness measurements using destructive methods are indicate by a vertical dashed line.	40
Figure 43.	Sectioning plan for the DED 316L SS component.	41
Figure 44.	Cross-section view of the sectioning plan showing the 4 mm wide specimens cut from the DED 316 L SS component.....	41
Figure 45.	Results for the optical wall thickness measurement at the 0° location. (a) Optical silhouette of the 4 mm wide strip section from the 0° location. (b) comparison of the NDE and optical wall thickness measurements and (c) amount of deflection from perfect straightness.	42

Figure 46.	SEM backscattered images obtained from the topmost region of a longitudinally cut specimen of the DED processed 316L SS cylinder.	43
Figure 47.	SEM backscattered montage image obtained from the bottom-most region of a longitudinally cut specimen of the DED processed 316L SS component.....	44
Figure 48.	SEM backscattered montage image of part of the bottom region removed from the 270° specimen. (a) EDS layered image of the solidification cells. Elemental maps of (b) iron, (c) manganese, (d) molybdenum, (e) nickel, and (f) chromium.....	44
Figure 49.	Liner built in progress at layer 951 and layer 1202, respectively	45
Figure 50.	Completed DED liner removed from the baseplate	46
Figure 51.	Dimensional measurements and comparison post deposition. (3D model based on nominal 0.088 minimum wall thickness. Comparison based on model “RPMI Modified_Liner for Complete Machining 1_stp” provided to PNNL on November 29, 2023)	46

Tables

Table 1. Manufacturing schedule to demonstrate powder geometry complexity effect on residual stresses and potential application windows6

Table 2. Microreactor concepts currently under development (Jackson, 2024)8

Table 3. Proposed characterization matrix for international geometry complexity benchmarks studies for geometric complexity effect and material compositional sensitivity effects 11

Table 4. Literature on DED 316L SSs and DED 316H SS data..... 12

Table 5. AM processing parameters used to fabricate 316H SS cube samples in this study 13

Table 6. 316L SS thermal material properties (Kim, 1975).....26

Table 7. 316L SS mechanical material properties (Nickel Institute, 2020, Sandmeyer Steel Company, 2014)29

1.0 Introduction

The Advanced Materials and Manufacturing Technologies (AMMT) Program focuses on developing cross-cutting technologies in support of a broad range of nuclear reactor technologies and to maintain U.S. leadership in materials and manufacturing technologies for nuclear energy applications. The overarching vision of the AMMT program is to accelerate the development, qualification, demonstration, and deployment of advanced materials and manufacturing technologies to enable reliable and economical nuclear energy. This project addresses the development of an initial non-proprietary component that can be used for benchmark studies between Generation IV International Forum (GIF) international members, that can be used to demonstrate the benefits of advanced manufacturing (AM) processes and gain knowledge, without sharing competitive information and therefore demonstrate integrated material and advanced AM processes for the microreactor industry which is one of the AMMT program's strategic collaborative targets.

1.1 Background

Developments in AM are occurring faster than the ability to introduce new materials and methods into design codes. Qualifying new AM technologies for use with nuclear design codes can be a long and complex process. The Generation IV International Forum (GIF) Advanced Manufacturing Materials Engineering Working Group (AMME-WG) was formed in 2018 as a task force and was strengthened to a working group in 2022 because of the continued interest and benefits identified for the nuclear industry and other stakeholders. The task force as well as the AMME-WG focuses on how collaborative AM research and development could be used to decrease time to deployment of Gen-IV advanced reactors. The nuclear community responding to the AMME task force and-WG surveys, doubled between 2019 and 2022, with the most recent 2023 survey showed that industry prioritization on AM technologies, components and materials changed significantly during the 5-year timespan, because although the number of participants are consistent, the trend has shifted from being interested in learning about applications of AM, toward more actively participating in development or pursuing the deployment of AM processes.

The key outcomes of the AMME-WG identified that the main barrier to wider adoption of AM materials and components is the lack of design, fabrication, and operating experience for AM technologies. While there is potential for AM techniques to have a disruptive impact on Gen IV reactors, the economic drive for parts manufactured using AM is currently quite low and overly restrictive regarding qualification or regulations might eliminate the economic case entirely. Lack of standardization of AM processes, covering the entire manufacturing and design process from feedstock to final parts, is a significant drawback compared to well-established conventional manufacturing techniques. Additionally, the nuclear industry can benefit from learning and adopting practices from more experienced sectors. However, a key takeaway from the October 2022 workshop in Toronto was that while the international community is eager to collaborate on demonstration and research activities, the sharing of proprietary information or designs often hinders progress. Therefore, a major decision was made by the AMME task force and subsequently the AMME-WG to develop a non-proprietary component that can be used for benchmark studies between international members, that can be used to demonstrate the benefits of AM processes and gain knowledge, without sharing competitive information.

Simultaneously, the AMMT program as part of the mission of the program is reported in the AMMT roadmap 2022 (Li et. al., 2022), supported through prior workshops/interactions from the previous Advanced Methods for Manufacturing (AMM), Nuclear Materials Discovery and Qualification initiative (NMDQi)-, and Transformation Challenge Reactor (TCR) programs, identify the need for demonstrations for accelerated adoption of AM products to the market.

During the latter parts of fiscal year (FY) 2023, the U.S. Department of Energy microreactor program's management, and specifically the MARVEL program manager, posed an AM challenge to the AMMT program to show feasibility of a full-scale disposal liner from 316H stainless steel (SS) as a demonstration of feasibility that it can be printed. Although such feasibility project is not covered in this report, as it is executed as part of other subprojects by Oak Ridge National Laboratory (Lister et. al., 2024) and PNNL, it is linked to this work package, as to benefit from the lessons learned from those development. Two versions of the liner assembly, one full-length and the other shortened, were printed from several materials (316L SS, Inconel 625, and Inconel 718) using four powder-based laser printers (BeAM Modulo 400 directed energy deposition [DED], EOS 290M laser powder bed fusion [LPBF], General Electric [GE] Concept Laser M2 LPBF, and GE Concept Laser Xline 2000R LPBF) located at the Manufacturing Demonstration Facility at Oak Ridge National Laboratory. The PNNL work scope included the printing of a full-scale liner from 316L SS using a DED manufactured at the RPM facilities and included funding for printing only that was completed during December 2023, as shown in Section 5.0.

1.2 Scope

This project addresses the development of an initial non-proprietary component that can be used for benchmark studies between GIF-international members. This benchmark can be used to demonstrate the benefits of AM processes and gain knowledge, without sharing competitive information. Furthermore, this can therefore demonstrate integrated material and AM processes for the microreactor industry, which is one of the AMMT program's strategic collaborative targets.

Specifically, the scope is to develop a benchmark study to include design, development, manufacturing, and performance measurement of agnostic reactor relevant geometries to support industry's adoption of AM in a variety of structures. Microreactor component geometries will be used as initial demonstration. Project activities will include performing structural analysis, establishing a characterization matrix, and initiating building from one material/process combination. The identification of agnostic geometries for different reactor types can provide reactor developers knowledge on the application space of new material/AM combinations to consider for future components by enhancing the Technical Readiness Level, thus familiarizing developers with the possibilities. Furthermore, using different geometry types will eliminate the hesitation of developers/industry to provide intellectual property and other proprietary component information to competitors. These geometries will be used in international benchmark studies, therefore expanding the pool of data.

Collaboratively, microreactor geometries were identified as suitable candidates for enabling LPBF and DED processes. The recent lessons-learned and needs from the MARVEL additive builds were used as a starting point. As no reporting was required for the full scaled Marvel liner built by RPMi for PNNL in December 2023 due to funding limitations, a summary is provided in this report, as 316L DED material is used as one of the benchmark options. Although this report also briefly discusses the vision of the GIF collaborative matrix, specifically the work of the U.S team (therefore the AMMT team) is discussed in this work with preliminary results provided.

2.0 Benchmark Study Development

The AMMT Program is to develop cross-cutting technologies in support of a broad range of nuclear reactors, and as mentioned, initial work was already performed on a microreactor Marvel liner component. The alignment and leveraging of the recent Marvel liner study has been the key influencer of the FY 2024 study, as the identified need and as work scope included only one set of technique and material type.

2.1 Identification of the AM Technique for the Benchmark Study

Powder DED technique has been identified as the technique for the FY 2024 benchmark study due to multiple reasons, namely:

leverage cylindrical sample pieces manufactured during the development stages of the full-scale DED 316L liner

- increased industry interest
- minimize overlap with the large investment in LPBF project scope of the AMMT program
- provide information to decrease the gap in knowledge and data for codes and standards
- interest from the international GIF community
- potential for complex parts with unique options to minimize weldments
- prevent overlap with the GIF Material board research projects that is currently been finalized.

By performing the benchmark study, the AMMT program will therefore provide the nuclear energy stakeholders with another manufacturing option and knowledge to apply for accelerated readiness for new or replacement designs, therefore accelerating the demonstration process.

The GIF-AMME-WG 2023 industry survey showed a significant increased interest in DED with 19 industry references to wire-fed DED and 15 to powder-fed DED, which is a significant increased interest compared to the survey conducted during 2023 (Figure 1). Furthermore, the AMMT program (Li et. al., 2022) has already significant investment in the acceleration and demonstration of LPBF (also listed in Figure 1 as one of the top 5 AM techniques), and nationally and internationally many organizations already perform research and development with demonstrations of applications, the AMMT program and the GIF-AMME WG decided to pursue both powder and wire DED as a manufacturing technique that can benefit nuclear energy stakeholders, in addition to LPBF. As the dimensional application space (as shown in Figure 2) and the specific features of the different additive manufacturing process are significantly different, the nuclear industry cannot only rely on one single manufacturing process to fulfil the supply chain requirement of components for new reactors and to sustain current reactors. Figure 2 shows the relative size component comparison between LPBF and powder DED, which also is one of the reasons for the interest by the industry community to the application of DED, as it also provides additionally the opportunity for more complex geometries and robotically features.

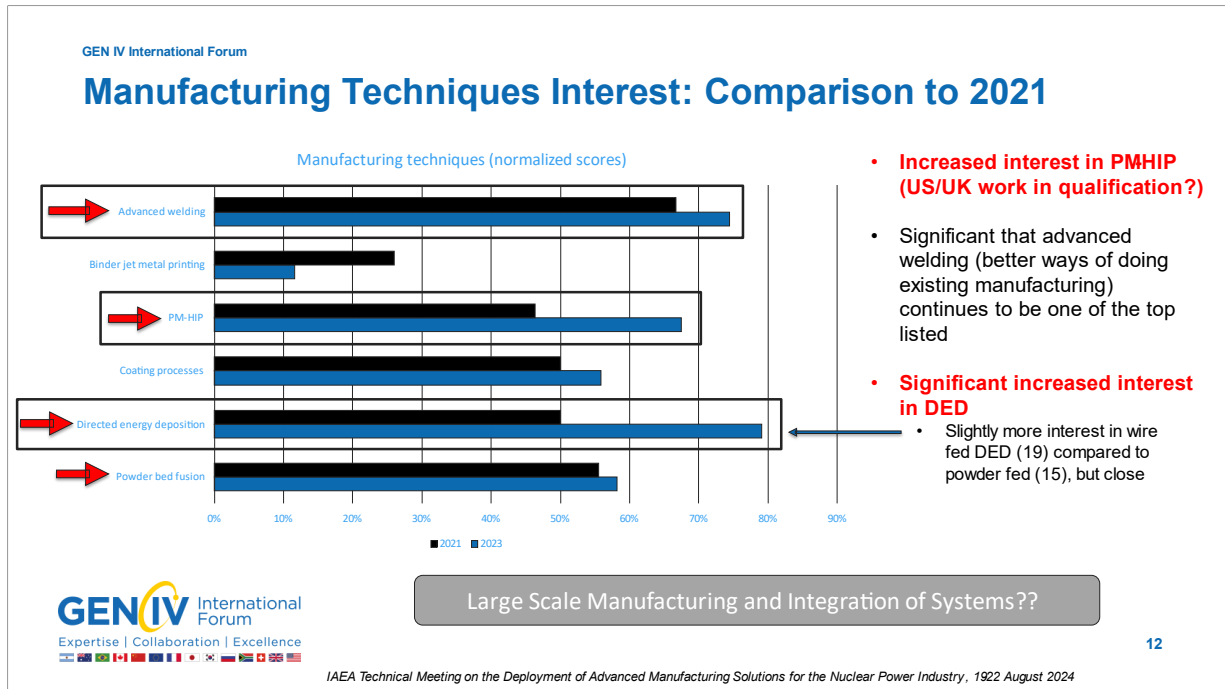


Figure 1. Industry interest in AM techniques based on the GIF-AMME WG 2023 industry survey (Van Rooyen, 2024)

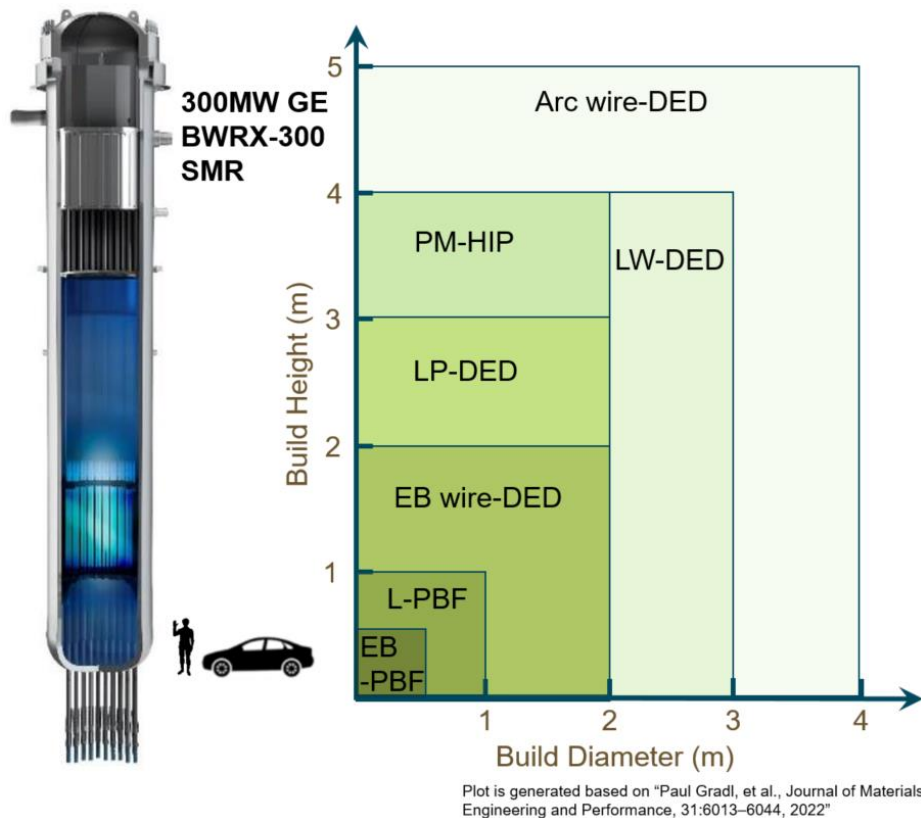


Figure 2. Dimensional application space for various AM processes as adapted from Gradl et. al., 2022

2.2 Identification and Motivation on the Material Type to be used for the Benchmark Study

Nuclear applications like in fuel cladding, nuclear powerplants, and nuclear pressure vessels need to be able to withstand highly thermal, radiological, and corrosive environments (Hensley et al., 2021; Nelson, 2023; Zhong et al., 2017). Stainless steels, particularly 316L SS, are good candidates for nuclear-based materials due to their high strength, good ductility, and corrosion resistance (Voisin et. al., 2021); however, for elevated temperatures, 316H SS has excellent creep and oxidation properties and therefore is a candidate for most first demonstrations of the generation IV reactor types. 316H SS has slightly higher carbon content (0.04%-0.10% C), which leads to higher strength than 316L SS (<0.03% C) (Doniger et. al., 2023). A corrosion study comparing 316L and 316H corrosion resistance showed after getting exposed to molten FLiNaK salt coolant, 316H had slightly higher corrosion resistance. The results suggested that the larger grain size in 316H reduces pathways for chromium dissolution, which in turn decreases the corrosion rate. Another possibility was due to the degree of sensitization occurring at higher temperatures where carbon reacts with chromium to create chromium carbide. Chromium diffusion decreases and is thermally stable. (Doniger et. al., 2023)

The selection of additively manufactured 316 SS as a case study for the AMMT program (Li et. al., 2022) was based on the developed material scorecards to prioritize for AM (Hartmann et. al., 2022). From nine materials considered, namely, 316 SS, 304 SS, Alloy 800H, Alloy N, HT9, Alloy 617, Alloy 718, Graphite C/C, and SiC composites, the assessment for light water reactors, sodium-cooled fast reactors, lead-cooled fast reactors, molten-salt reactors (MSR), very-high temperature reactors, and microreactors showed that additively manufactured austenitic steel grades 316L SS and 304 SS were most promising for nuclear deployment and had the highest level of overall maturity and readiness level (Figure 3).

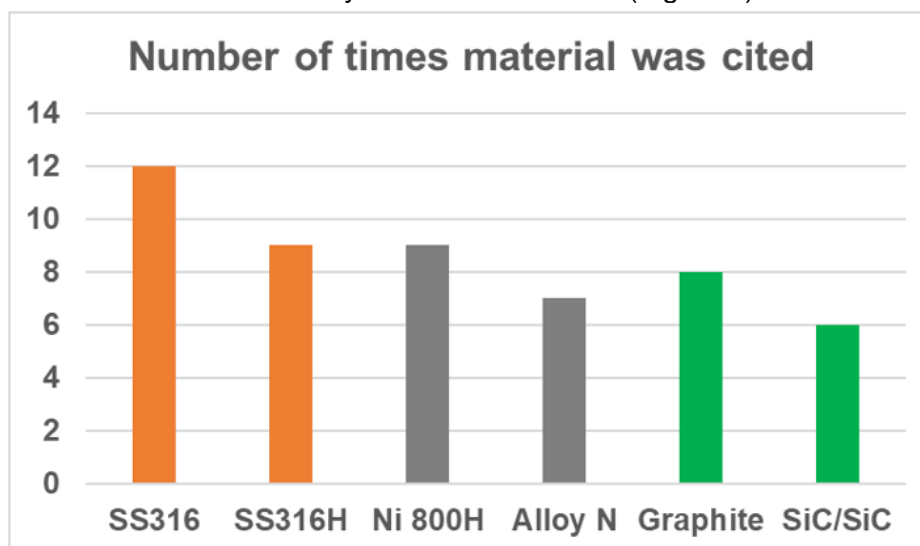


Figure 3. Number of times a material was referenced by survey participants as a candidate for AM for nuclear application (Hartmann et.al., 2022)

In collaboration with the other GIF member country members of the GIF-AMME WG, different variations of 316 SS were highlighted as the preferred alloy type to consider for the benchmark study. This will provide a new database and comparative dataset for the international industry and will benefit the larger nuclear stakeholders by understanding the variations and the possible

impact it may have on the different reactor type applications. The alloy variants that will be considered by the larger international benchmark study will be 316L, 316H, 316H (low N), 316L (low N). The AMMT program, therefore the U.S. members of the GIF-AMME WG, is focusing on the 316H and 316L SSs with selected experimental work on the 316H SS (low N).

Specifically, following is the rational and acceptance from an international subject matter experts for the choices: *“Ansaldo Nucleare is monitoring all AM processes. L-DED lacks a set of ISO/ASTM industrial standards, which are instead available for LPBF. Just to make an example, ASTM F3184 for LPBF 316L components exists, but there is no equivalent standard for L-DED. Personally, I think that L-DED has a good potential in nuclear applications, because it would enable to build larger components compared to LPBF (extending AM application in RPV internals, for instance, where we know that geometries are complex, or to other NPP components).”* The expert further indicated that we as a GIF-AMME-WG team can “contribute with research activities in creating a background for industrial standards dedicated to L-DED”, which will further enhance the application for AM for larger scale products.

2.3 Identification and Motivation of the Geometries to be Used for This Benchmark Study

A schematic view of the simplistic geometries (cube to cylindrical components) chosen for the benchmark study is shown in Figure 4 with the material relevant matrix shown in Table 1. The relevant microreactor components evaluated to prepare the non-proprietary design is discussed in Section 2.4. Although the benchmark starts initially with simplistic cubical and cylindrical forms, it builds up to a mock-up of a non-proprietary design, that can demonstrate a variety of features that can be useful to present knowledge to specific designers of micro reactors and for that matter also for other reactor type designers. The initial cubical and cylindrical forms are steps to obtain surface features and dimensional responses to the identified process parameters to be used in the non-proprietary design mockup. The current powder DED work performed by PNNL on 316H SS is identified by “B” and “C” in the Table 1 and the future work by PNNL in FY 2025 is showed with a “D”. The “?” indicates that the confirmation and detailed planning with the international community as part of the GIF-AMME-WG is still in progress to be confirmed.

Table 1. Manufacturing schedule to demonstrate powder geometry complexity effect on residual stresses and potential application windows

	Cube	Solid Disk	Tube/Small-Diameter Cylinder	Large-Diameter Cylinder	PNNL Non-Proprietary Design: Mock-Up	Full Scale Micro Reactor Heat Exchange Liner
316L	? A TBD	?A TBD	B Nov 2024	C Dec 2023	? A TBD	C Dec 2023
316LN	A	A	A	A	A	N/A
316 H (low N)	C July 2024	B Nov 2024	B	B	A	N/A
316 H	? A, D*	A	? A D	? A, D	? A, D	N/A

A: Proposed for AMME WG
B: PNNL in process
C: PNNL
D: PNNL FY25 using LPBF
* Only confirmatory based on the AMMT program qualification tests

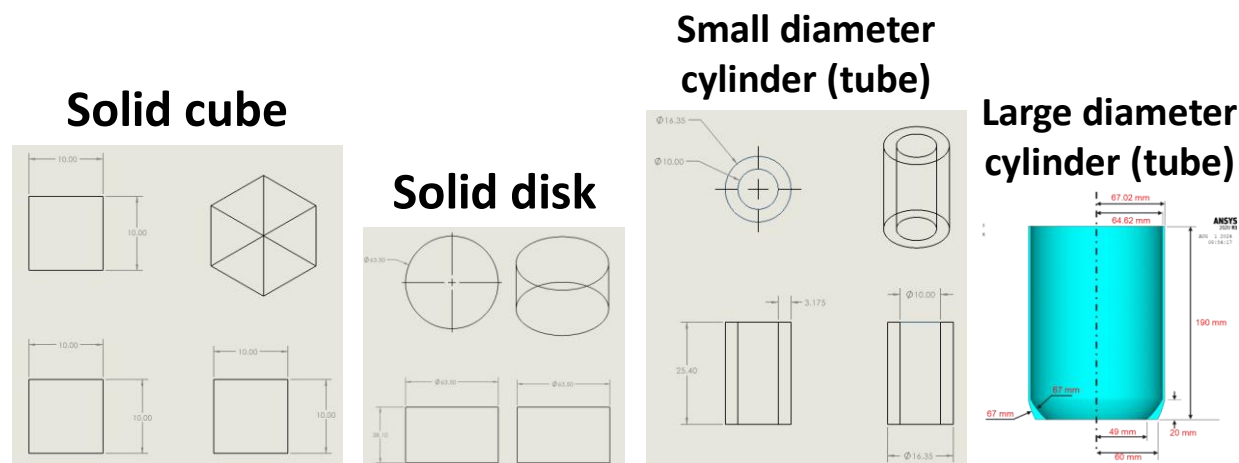


Figure 4. Dimensions of the benchmark samples identified in Table 1

2.4 Evaluation of Advanced Reactor Geometries and Design of Agnostic Non-Proprietary Mock-Up Component for the Benchmark Study

Over the past several years there has been growing interest from the U.S. Department of Energy on the development of microreactors. Microreactors are compact nuclear reactors small enough to transport via ground transportation methods, like shipping containers, which enable them to be used in remote or underdeveloped areas. The development of these microreactors, provides a unique opportunity for the application of additive manufacturing technologies, such as DED and LPBF, to manufacture reactor components. There are several microreactors that are currently in development that are outlined in Table 2. A recent presentation by Jackson 2024, shows examples of typical microreactor components in Figure 5 and Figure 6. Due to the small size constraints for these microreactor designs, it is crucial that all available space is optimally used. This makes additive manufacturing technologies like DED and LPBF, prime candidates to produce complex parts at reduced costs and materials compared to traditional manufacturing methods. This project aims to select a common microreactor component, that is traditionally costly and difficult to make, to be manufactured through DED. To ensure a quality build that exhibits minimal residual stress, finite element analysis (FEA) of the build process will be utilized to identify key process parameters, such as build path, spot size, and scan speed. Once the part is built, residual stress measurements will be conducted through non-destructive evaluation (NDE) techniques. The residual stress data will then be used to calibrate the FEA models to improve accuracy. The development of the proposed FEA models will provide a cost-effective process for the development of new microreactor components to be additively manufactured through DED.

This project has identified several potential common components that could be additively manufactured through DED, which include expanded elbow pipe, guard vessels, Stirling engines, heat exchangers, pumps, and valves. Figure 7 - Figure 11 display a few examples of these potential common microreactor components. This project proposes using an expanded pipe leading into an elbow as the selected component, shown by Figure 7. This component is not only extremely difficult and costly to manufacture through traditional methods, it also can reduce space needed for traditional transition areas. This design allows for a smooth transition from a larger pipe to a smaller pipe at the location of a 90° bend and has potential to increase

fluid flow and reduce turbulence. Thus, the expanded elbow pipe is an excellent candidate for demonstrating the ability to use DED for manufacturing of microreactor components.

Although there are zero publicly available microreactor design schematics, one can infer the sizing for the parts. Standard shipping containers are 8ft x 8.5ft x 20ft. Thus, it is reasonable to assume that the max pipe diameter would be 2ft in diameter, with most of the piping being 1ft in diameter and smaller. It is proposed that the approximately dimensions for the expanded elbow pipe have a 1ft ID at the larger end with 0.375in. wall thickness, and a 6in. ID, 0.625in. wall thickness at the smaller end. The proposed approximate flange size has a 16in. OD at the larger end and a 10in. OD at the smaller end, with flange thicknesses of 0.5in. These dimensions are simply realistic placeholders that can easily be changed to fit microreactor design needs.

Table 2. Microreactor concepts currently under development (Jackson, 2024)

Developer	Reactor Name	Type	Fuel	Coolant	Moderator
Aalo Atomics	Aalo One	STR	U-Zr-H	Sodium	H
Alpha Tech Research Corp	ARC Nuclear Generator	MSR	LEU	Fluoride salt	
Antares Industries		Heat Pipe		sodium	graphite
BWXT	BANR	HTGR	TRISO	Helium	graphite
General Atomics	GA Micro	HTGR		gas	
HolosGen	HolosQuad	HTGR	TRISO	Helium/CO2	
Micro Nuclear, LLC	Micro Scale Nuclear Battery	MSR/heat pipe	UF4	FLiBe	YH
Nano Nuclear	Zeus/Odin	HTGR/MSR	UO2	Helium	
NuGen, LLC	NuGen Engine	HTGR	TRISO	Helium	
NuScale Power	NuScale Microreactor	LMTM/heat pipe	metallic	Liquid Metal	Liquid Metal
Oklo	Aurora	SFR	metallic (U-Zr)	Sodium	
Radiant Nuclear	Kaleidos Battery	HTGR	TRISO	Helium	graphite
Ultra Safe Nuclear	MicroModular Reactor	HTGR	TRISO	Helium	graphite
Westinghouse	eVINCI	heat pipe	TRISO	Sodium	graphite
X-Energy	XE-MOBILE	HTGR	TRISO	Helium	graphite



Figure 5. Example of guard vessel (Jackson, 2024)



Figure 6. Schematic of the internal heat exchangers within the MARVEL Microreactor (Laboratory, 2022)

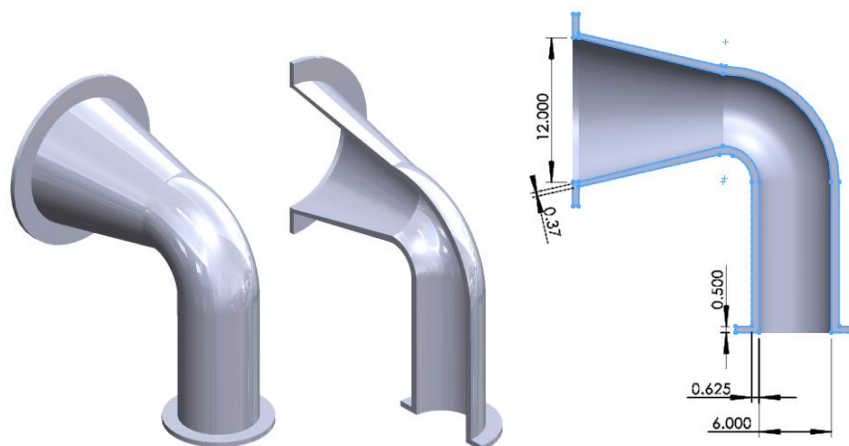


Figure 7. Draft schematic of expanded elbow pipe (dimensions are in inches)



Figure 8. Initial draft schematic of two-axis pipe



Figure 9. Example graphic of flanged elbow pipe without expansion (MDC Precision, 2023)



Figure 10. Example Schematic of Pump Impeller (Orye, 2021)

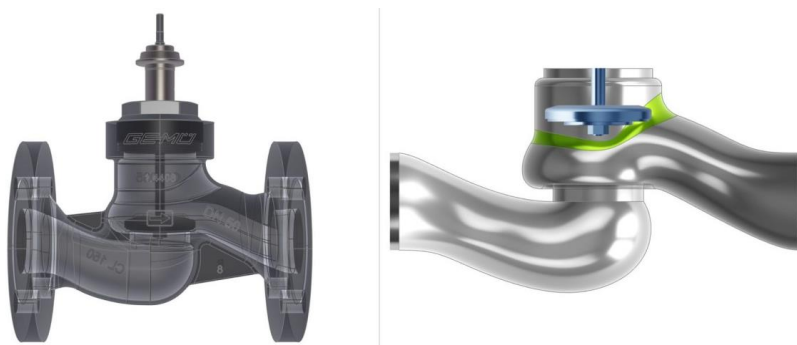


Figure 11. Example schematic of check valve (Khan, 2023)

2.5 Identification and Motivation of the Characterization or Performance Testing to be used for this Benchmark Study

Although all the demonstration activities have not been fully confirmed and planned, the initial proposed characterization and testing matrix are shown in Table 3 with the “X” confirmed for the DED 316H samples only.

Table 3. Proposed characterization matrix for international geometry complexity benchmarks studies for geometric complexity effect and material compositional sensitivity effects

	Cube		Solid Disk		Tube/Small Diameter Cylinder		Large Cylinder		PNNL Non-Proprietary Design		Full Scale Micro Reactor Heat Exchanger Liner	
Powder Characterization	X		X		X		X		X		X	
Optical Microscopy - Porosity	A, X		A, X		A, X		A, X		A		A	
Density	A, X		A, X		A, X		A, X		A		A	TBD
SEM - EBSD GBC, KAM, Orientation	A, X		A, X		A, X		A, X		A		A	TBD
XRD - Phases - Residual Stresses	A, X		A, X		A, X		A, X		A		A	TBD
Hardness RT→800°C	A, X		A, X		A, X		A, X		A		A	TBD
Mechanical properties Tensile & Yield Strength RT →800°C	B		N/A		A		A		A		A X	TBD
Creep and/or Creep *												
Fatigue RT → 800°C	? B	TBD	N/A		A		A		A		A X	TBD
NDE	C		C		C		C		C		C X	TBD
Environmental Testing	? B	TBD	? B	TBD	? B	TBD	? B	TBD	? B	TBD	X	TBD

A: Small sample from actual part

B: Separately Standard Size Fabricated Sample

C: Full actual part

D: PNNL planned or completed

* Only confirmatory based on the AMMT program qualification tests

Specifically, the NDE testing will be developed by the GIF AMME WG task lead as a separate task at a later stage, but as part of this work, it will include defect and potential surface effects evaluation in complementary activities of another work package of the AMMT program.

3.0 316H Stainless Steel Survey and Cube Preliminary Evaluation

This section discusses background information used to determine the experimental process parameters for the printing of the 316H SS with the powder DED process with some reference to differences between the printing of this material with LPBF and LP-DED. Although the characterization of the experimental samples is only reported preliminary in this report, a brief survey is also included to discuss some of the characterization methods that was considered for determining the experimental matrix in Table 3.

3.1 316L and 316H Powder DED

Most 316H SS studies have focused on creep properties, thermal cycles, basic mechanical property testing via tensile testing and hardness testing, and microstructure analysis. 316HSS studies heavily investigate creep strain rate. An important relationship between creep strain and stress triaxiality was made and modeled to represent real-life creep stress and strain conditions (Yatomi et. al., 2004; Hares et. al., 2018). However, very few studies have focused or looked at the use of 316H SS in MAM DED and process parameter optimization (DeNonno et. al., 2024; Gonzalez, Tate, and Klemm-Toole 2023)

Understanding of process parameters such as laser power, scanning speed, scanning strategy, etc., are needed to be investigated to understand their effects on densification, porosity, and microstructure. Studies have shown high porosity levels facilitate crack propagation (Herzog et. al., 2016; Piscopo and Iuliano 2024). Porosity in 316LSS decreased while increasing laser power and travel speed (Yadollahi et. al., 2015). In Figure 12, several 316L SS studies point evidence to increased laser power to lowering porosity. Porosity mitigation is possible by adjusting laser power, scan speed, and laser energy density (Svetlizky et. al., 2021). Powder feedstock composition and quality also plays a factor how porosity is introduced into printed parts. Idle time in DED processes affects porosity. Hwang et. al., 2023, 316L SS DED study measured 0.13-0.60% porosity in the printed samples. They determined the deposition strategy greatly influenced the porosity. From their results, the best strategy was using a raster deposition path rotated 67° at each layer and without the use of an idle time (Hwang et. al., 2023). However, knowledge of the process and 316H SS's relationship among DED process parameters along with the microstructure and mechanical properties have not been greatly investigated. This 316H SS DED study investigates the effect of laser power and scan speed on the relative density and microstructural porosity (summary in Table 4).

Table 4. Literature on DED 316L SSs and DED 316H SS data

Machine	Alloy	Laser Power (W)	Scan speed (mm/s)	Porosity (%)
Optomec LENS® 3D Hybrid 20(Amar et. al., 2023)	316L	250/475/700	3.3/6.7/10	0.5-12
Optomec LENS MR7 (Izadi et. al., 2017)	316L	100/200/250	8.5/12.7/17	0.5-18
Optomec LENS 850M (Sciammarella and Salehi Najafabadi 2018)	316L	645	2.1-19	1.1

Machine	Alloy	Laser Power (W)	Scan speed (mm/s)	Porosity (%)
Optomec LENS 750 (Yang et al. 2016)	316L	360	16.3	-
Optomec LENS 750 (Yadollahi et. al., 2015; Yadollahi et. al., 2016)	316L	360	8.5	2.6-3.4
Optomec LENS MR7 (Ziętala et. al., 2016)	316L	400	15	-
Optomec LENS MR7 (Hwa et. al., 2021)	316L	380	-	0.05-0.83
Optomec LENS	316H	400/500/600/700	600/700/800/900	0.030-0.84
* Data taken from our 316H SS study (Table 5)				

Table 5. AM processing parameters used to fabricate 316H SS cube samples in this study

Sample	Power (W)	Scan Speed (mm/min)	Hatch spacing (mm)	Relative Density (%)
1	400	600	0.9	99.668
2	400	700	0.9	99.160
3	400	800	0.9	99.591
4	400	900	0.9	99.599
5	500	600	0.9	99.958
6	500	700	0.9	99.960
7	500	800	0.9	99.900
8	500	900	0.9	99.555
9	600	600	0.9	99.880
10	600	700	0.9	99.918
11	600	800	0.9	99.904
12	600	900	0.9	99.938
13	700	600	0.9	99.936
14	700	700	0.9	99.970
15	700	800	0.9	99.962
16	700	900	0.9	99.668

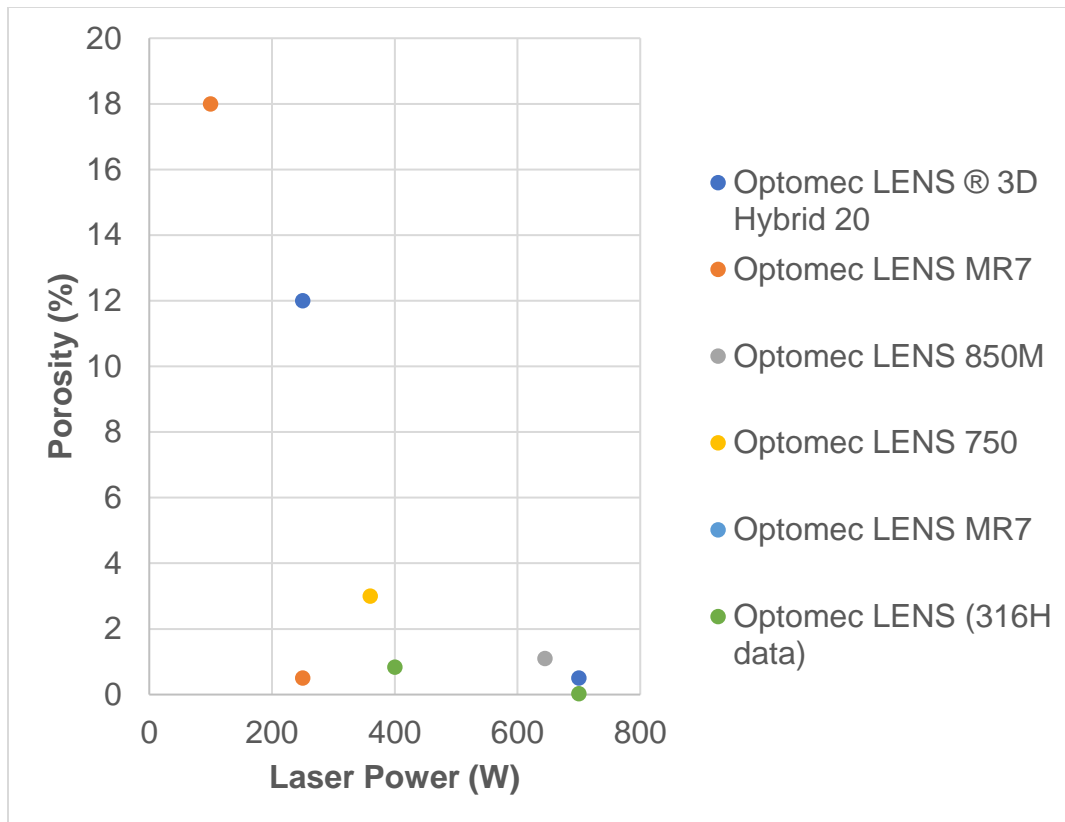


Figure 12. DED Optomec LENS machine study data on laser power and porosity

3.2 Residual Stresses: Origin, Mechanism, Process Parameters that Affect Lower or Higher Residual Stress Output

Residual stresses originate in the melted powder or wire area known as the melt pool, which undergoes a rapid thermal heating/cooling process. After the current layer has been melted and cooled, the next layer is set up and powder is deposited onto the newly formed layer. The laser beam moves directly above the cooled layer along the scanning direction and moves with defined spot size and point distance. The melted powder layer expands across subjacent to the cooled layer below, creating a non-uniform temperature gradient. The cooled layer restricts the melting flow expansion by creating compressive forces, generating compressive stresses. The upper part of the cooled layer counteracts by applying opposing forces, creating tensile stresses, which results in tensile stress on the lower part of the cooled layer to counter act the compressive stresses. After expansion, the melted layer rapidly cools at a faster rate than the layer subjacent to it, generating tensile stresses. As seen in Figure 13, this results in permanent plastic deformation due to lattice strains and subsequently, residual stresses. (Bartlett & Li, 2019; Mercelis & Kruth, 2006)

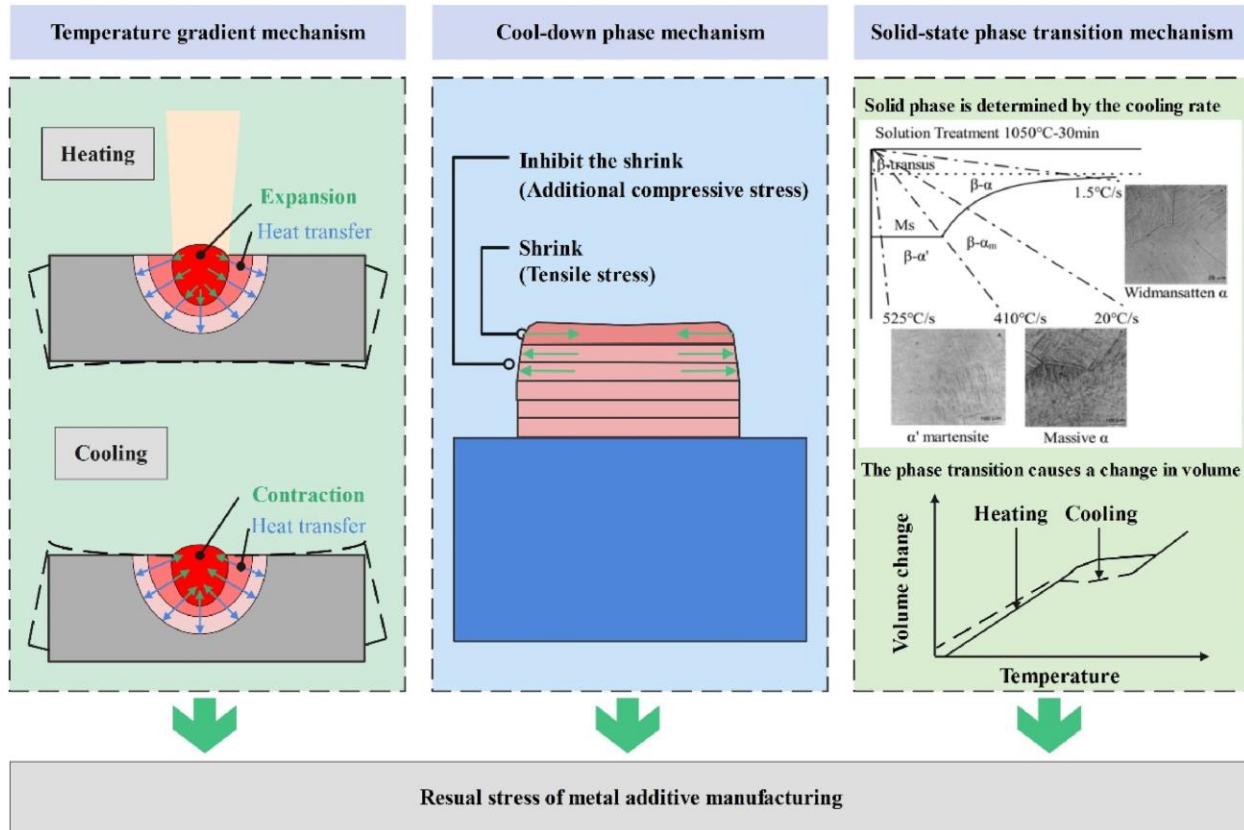


Figure 13. Mechanisms of residual stress formation in MAM. Note. Reproduced from Chen, et. al., 2022. CC-BY

Residual stresses affect MAM part fabrication and geometry such as cracking and warping. In addition, it has a significant impact on corrosion resistance, microstructure, and mechanical properties of the material. (Chen et. al., 2022; Romano et. al., 2018). Zhang et al., 2020 discusses how residual stresses in DED affect tensile stresses as higher residual stresses causes higher compressive stresses to resist crack propagation (Huang et. al., 2009; Moon et. al., 2018; Zhang et. al., 2020). Zhou et al., 2020 studied corrosion resistance in LPBF 316L SS samples and found residual stresses affect corrosion resistance due to the formation of melt-pool boundaries, creating additional inner compressive stresses (Zhou et al., 2020). Residual stresses are affected by MAM process parameters. MAM review studies find laser power, scanning speed, scan strategies, melt pool size, thermal gradient, and material type all impact residual stress (Chen et. al., 2022).

3.2.1 Laser Powder Bed Fusion

Kruth rescanned each individual layer of 316L SS printed selective laser melting (SLM) and reduced the residual stresses (Mercelis & Kruth, 2006). The residual stresses in the LPBF printed parts increased by increasing the number of printed layers from 50 to 300 layers (Mercelis & Kruth, 2006). Wu et al. used LPBF in conjunction with different scanning strategies to measure residual stresses in 316L SS samples. They found the residual tensile stress was reduced by using a smaller island size from 5 mm by 5 mm to 3 mm by 3 mm.

An example of island scanning strategy is seen in Figure 14. Residual tensile stresses were reduced by increasing the laser power/scanning speed ratio (Chen et. al., 2022; Wu et. al.,

2014). Yadroitsev & Yadroitsava, 2015 used selective laser melting (SLM) to print 316L SS samples and saw higher residual stresses along the scanning direction (Yadroitsev & Yadroitsava, 2015).

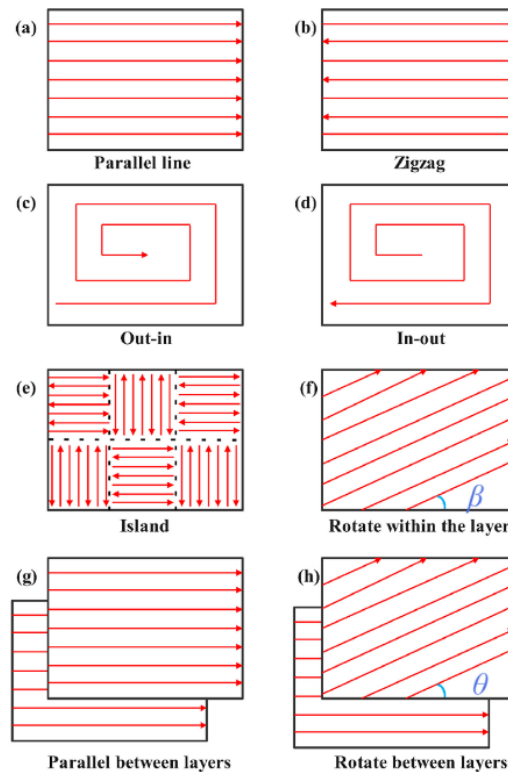


Figure 14. Scanning strategy for MAM. (a)-(f) Scanning strategy in a single layer; (g) and (h) relationship between layers. Note. Reproduced from Chen, et. al., 2022. CC-BY

The study conclude higher laser power will lead to greater residual stress. Mugwagwa et. al., 2018 saw using a combination of a higher laser power and lower scanning speed in LPBF can reduce residual stresses but attain good part relative density (Mugwagwa et. al., 2018). However, it is evident the process parameters still need to be optimized based on part geometry and size. Reducing the scanning speed is like increasing the power of the heat source. A higher laser power will generate a larger melt pool, thus increasing heating temperature and cooling rate. In addition, the melt pool's volume shrinkage during cooling will be larger, generating higher residual stress (Hussein et. al., 2013; Liu et. al., 2016). In tandem, this also causes a significant decrease in the density of the sample, and the porosity may relax the residual stress (Simson et. al., 2017).

3.2.2 Direct Energy Disposition

Piscopo et. al., 2021 conducted a 316L L-DED process parameter study by varying laser power and scan speed. Their results found that either increasing laser power decreased residual stresses due to a lower thermal gradient value or decreasing travel speed decreased residual stresses due to a smaller melt pool and greater interaction between the laser and material (Piscopo et. al., 2021). Lu et. al., 2021 and Wei et. al., 2021 discuss how DED techniques directly print onto the substrate with no support structures, whereas LPBF such as SLM uses support structures. The high substrate rigidity increases residual stresses (Lu et. al., 2021; Wei et. al., 2021). Ding et. al., 2023 conducted a DED scanning strategy study and their effects on

residual stresses and deformations. Through experimental testing and verification using a thermodynamic finite element model (FEM), they found the “zig-zag” scanning pattern was the most minimal substrate deformation and lower residual stresses (Ding et. al., 2023).

3.2.3 Unique differences between DED vs. LPBF in 316L SS

DED uses a localized heat source and repeated deposition layers, resulting in repeated and rapid heating/cooling processes in every layer of a single part. This results in recurrent heterogeneous microstructure formation along with the energy stored in distorted grains, creating a non-uniform microstructure in DED components, resulting in residual stresses. DED processes use higher laser power and slower scanning speeds than LPBF. This leads to more significant heating of the underlying substrate and previously deposited material. In addition, with the absence of a powder bed in DED, heat cannot be conducted away as easily. This leads to greater heat retention. Overall, the interlayer deformations must withstand severe heating cycles in DED than in LPBF (Kumaran et al., 2021; Mithal et. al., 2024). Kumaran et. al., 2021 reported a higher residual stress value in the DED sample compared to the LPBF sample. Pacheco et. al., 2022 conducted a 316LSS DED study and saw the thermal stresses resulted in higher residual stresses, resulting in higher microhardness values (Pacheco et. al., 2022). Piscopo et. al., 2021 comments DED has higher residual stresses due to higher heat input and inability to control the substrate temperature (Piscopo et. al., 2021). From these studies, it is more desirable to choose LPBF over DED to avoid additional sources of thermal stresses and absence of more highly localized areas of thermal gradients.

3.3 Methods for Determining Residual Stresses

Methods to determine and characterize residual stresses can be done non-destructively or destructively. (Mugwagwa et. al., 2021)

3.3.1 Neutron Diffraction and X-Ray Diffraction

Imaging techniques such as neutron diffraction (ND) and X-ray diffraction (XRD) measure the distance between lattice spacings within the sample’s microstructure. ND’s advantage is its ability to penetrate larger depths into the material, as opposed to XRD which can only take surface-level diffractions (Schröder et. al., 2021). ND can penetrate steels between 20-30 mm (Dai et. al., 2008), whereas XRD can only penetrate several microns (Noyan et. al., 1995). Another study reported about 0.2 mm (Rossini et. al., 2012). In ND, a monochromatic neutron beam at the sample, spreading the neutrons and projecting a diffraction pattern, as seen in Figure 14. The diffraction pattern determines the changes in lattice spacing. The elastic strains are derived from the changes in lattice spacings of the crystalline material using Bragg’s law, generating a strain map. The stresses are calculated through the incorporation of the elastic properties of the material given by Hooke’s law. (Lee et. al., 2024; Measurement of Residual Stress in Materials Using Neutrons, 2005). An advantage ND has is the ability to get all three orthogonal strain components to calculate the full residual stress fields, whereas XRD can only find two components, limiting the analysis (Phan et. al., 2019; Rossini et. al., 2012). One downside to ND is lack of spatial resolution, thus might not have the ability to detect fatigue in samples on the surface (Phan et. al., 2019).

Similarly, XRD detects and measure the distance between lattice spacings within the sample’s microstructure. However, XRD is limited as it can only penetrate at the surface, not in large depths. A monochromatic X-ray beam is shot onto the sample, projecting a diffraction pattern, similar to Figure 15. The diffraction pattern picks up the diffraction peaks, which corresponds to

the lattice planes (Figure 16 [Huan et. al., 2020]). The stressed lattice spacings are measured using Bragg's law based on the X-ray beam wavelength, plane angle, and lattice spacing. Strains are calculated relative to the stress-free lattice spacings. Hooke's law is used to calculate the compressive and tensile stresses. (Zhang et. al., 2023). ND and XRD can be verified using FEM.

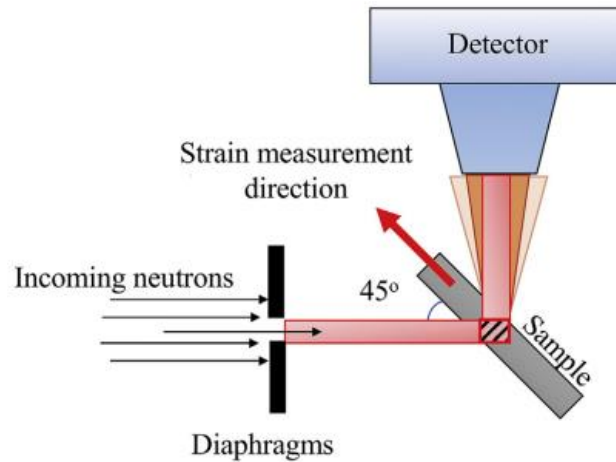


Figure 15. Neutron diffraction schematic of a sample measurement setup. Note. Reproduced from Goel et. al., 2020. CC-BY

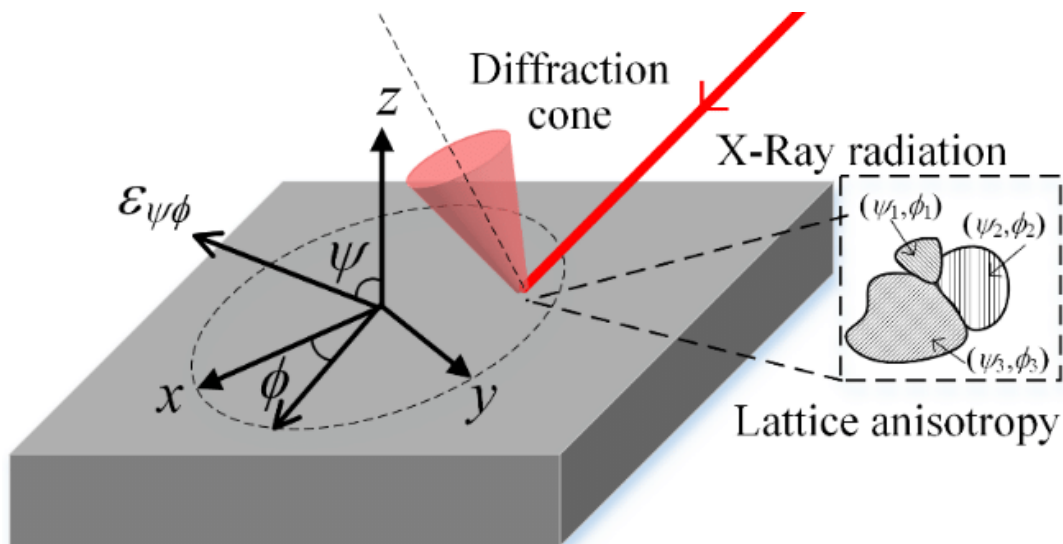


Figure 16. X-ray diffraction schematic to determine residual stresses. Note. Reproduced from Huan et. al., 2020. CC-BY

3.3.2 Digital image correlation (DIC)

DIC is a non-destructive experimental method to measure residual stresses in LPBF using three-dimensional digital image correlation (3D-DIC) to capture in situ surface distortion and residual strains before and after deformation. Polyzos et. al., 2023 quantified residual thermal stresses using experimental DIC images with FEM. 316L SS parts were printed as an inverted

cone geometry with L-DED. They are then used to measure the thermal expansion coefficient of thin-wall specimens and predict the displacement field from the hole drilling method to estimate and calculate the residual stresses, as seen in Figure 17.

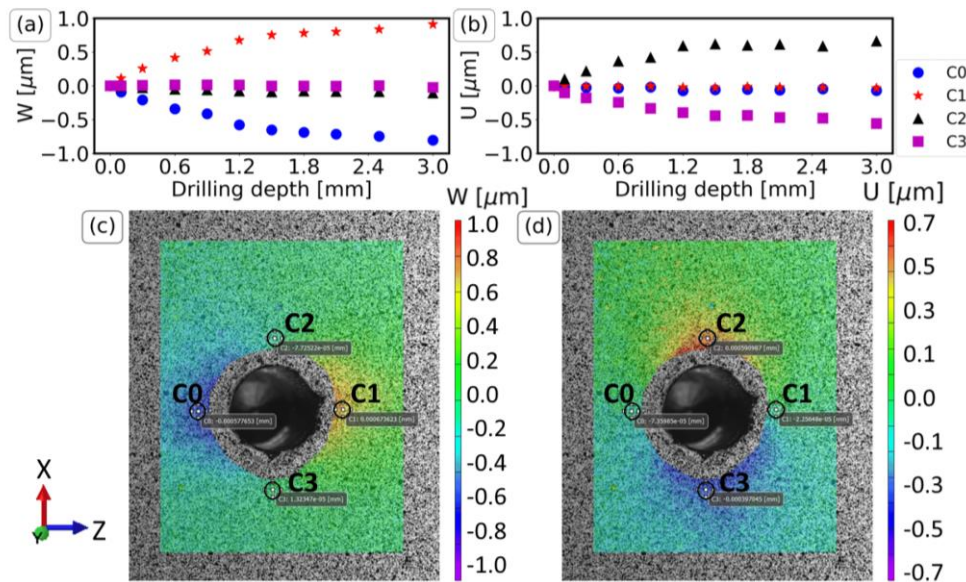


Figure 17. DIC results of the displacements W (a,c) and U (b,d) for the four points C0, C1, C2, C3. The plots (a,b) presents the average value for various drilling depths. The contours (c,d) as seen in VIC-3D, illustrate the displacement field for a drilling depth of 1.2 mm. Note. Reproduced from Polyzos et. al., 2023. CC-BY

The residual stresses are calculated using 3D surface measurements before and after performing AM. They found a heterogeneous distribution of residual stresses due to dynamic cyclic nature of heating and cooling of the new layers. FEM was able to validate the heterogeneous development of residual stresses. With more layers added, the stress state became more heterogeneous (Boruah et. al., 2023). From experiments, the residual stresses are highly dependent on part geometry. The study concluded that the DIC methodology has the necessary precision to evaluate the development and distribution of features in AM parts. In Bartlett et. al., 2018 SLM study, they developed a 2D analytical model to convert DIC surface curvature measurements to estimates of in-plane residual stresses. Experimental validation using 316L SS “inverted-cone” parts demonstrated that residual stress varied across the surface of the printed part, and strongly interacted with the component geometry. The 3D-DIC based RS measurements were validated by XRD with an average error of 6% between measured and analytically derived stresses. Calculations showed that the heterogeneous RS distribution in the parts emerged from the sequential re-heating and cooling of the new surface, and changed dynamically between layers (Bartlett et. al., 2018). From the two studies, both were able to conclude part geometry plays a significant role in residual stresses measurements.

3.3.3 Hole drilling, crack compliance, and contour tests

As seen in Figure 18., destructive testing can characterize residual stress by the hole drilling method, the crack compliance method, and the contour method. Both methods relieve residual stresses. In the hole drilling method, holes are incrementally drilled to create stress-free surfaces and elastic deformation. The deformation is measured and is used to calculate the residual stresses prior to hole drilling (Bobzin et. al., 2020; Roehling et. al., 2019; Strantza et.

al., 2019). Similarly, in the crack compliance method, the part gets cut with a small slit to relax the residual stresses. The residual strains before and after are measured with strain gages attached to the part (Roehling et. al., 2019). In the contour method, a cut is made into the sample and the resulting displacements are measured within the cross-sectional area and used in a finite element model to estimate the residual stresses (Prime, 2000; Woo et. al., 2013).

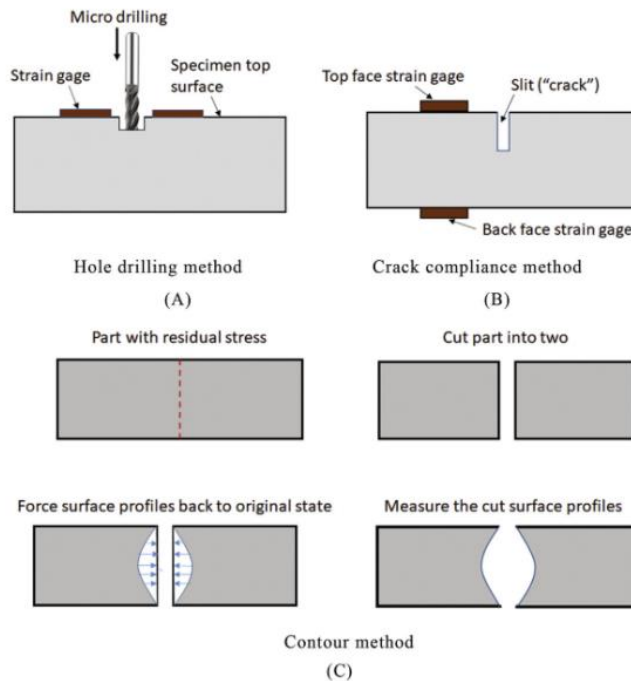


Figure 18. Measurements of residual stress by hole drilling (A), crack compliance method (B), and contour method (C). Note. Reproduced from Roehling et. al., 2019. CC-BY

3.3.4 Electron backscattering diffraction (EBSD)

EBSD is a scanning electron microscopy (SEM) technique which can characterize the crystallographic orientation, lattice crystal type, and microstructure.

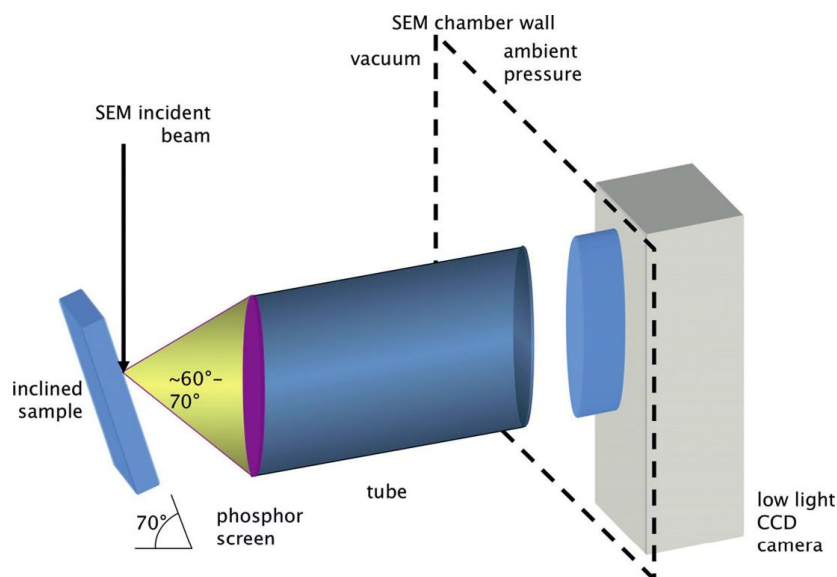


Figure 19. Schematic diagram showing the experimental set-up for EBSD observations. Note. Reproduced from by Wilkinson and Britton, 2012 CC-BY.

As seen in Figure 19, this is done by using a probe which focuses electrons onto a sample's tilted surface and backscattered from the sample which are collected by a photon imaging detector which creates the patterns. The patterns are indexed, and Hough transform is applied to locate peak positions. The patterns are then converted to identifiable angles and phases within the sample of interest (Wilkinson & Britton, 2012). EBSD patterns are useful in their ability to identify and measure elastic and plastic strain. By performing EBSD on an unstrained and strained material and comparing and measuring both patterns, the components of the strain tensor can be determined using cross-correlation and the Kikuchi band shifts (Wilkinson et. al., 2006). An application of EBSD is estimating the residual strains of a strained material by measuring "misorientation" angles corresponding to the material's plastic strains. Wright et. al. (2011) describes a "local misorientation approach" in which residual strains can be measured from lattice dislocations within a grain boundary by examining boundary angles and the corresponding Geometrically Necessary Dislocation (GND) density. The local misorientations can determine a material's strain distribution using kernel average misorientation (KAM). The KAM method averages all the misorientations values (ϕ) within a kernel instead of a single grain. (Wright et. al., 2011). Studies using EBSD KAM will be performed on selected samples in future work.

3.4 316H Stainless Steel Cube Samples: Preliminary Results

Sixteen 316H SS cube samples (Figure 20 and Figure 21) were fabricated utilizing process parameters indicated in Table 5. Sample porosity was imaged using SEM. The effect of laser power and scan speed on porosity is evaluated in Figure 22 and Figure 23.

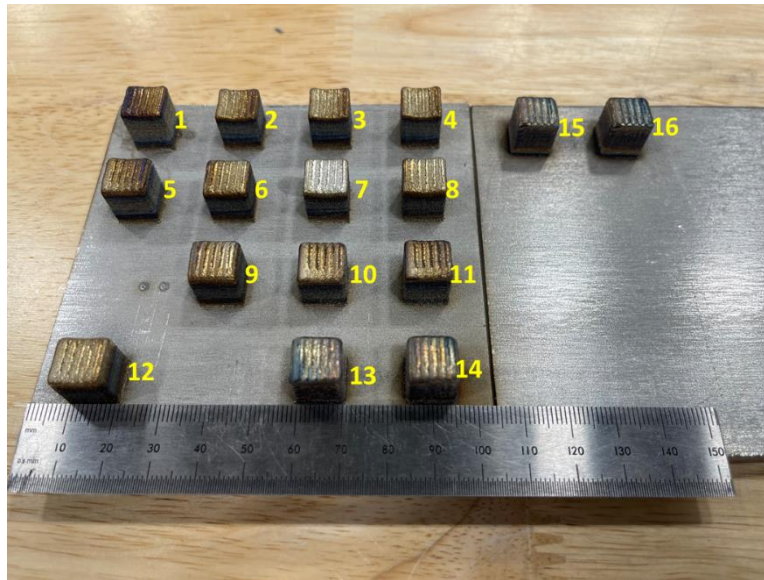


Figure 20. Sixteen individually DED fabricated cubes of 316H SS.

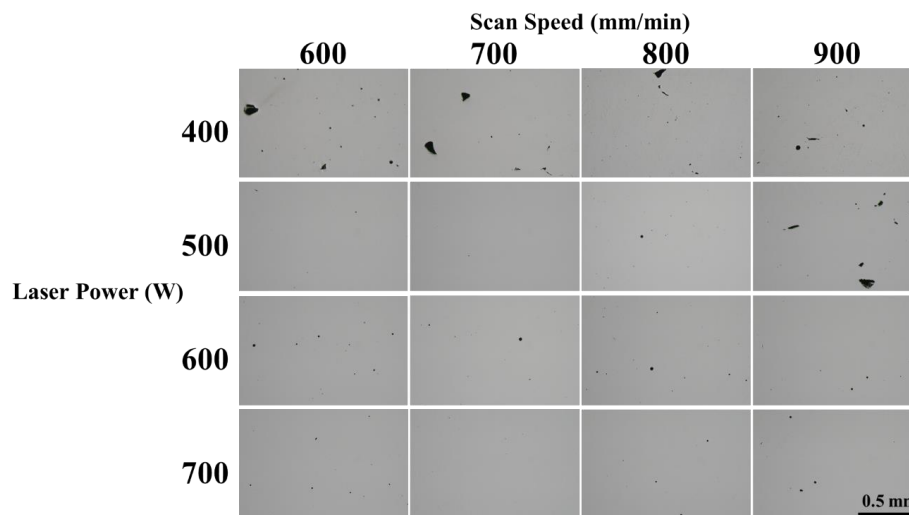


Figure 21. Optical micrographs of the XZ cross sections of 316H SS samples produced at various laser power and scan speeds

In Figure 22, as scan speed increases from 600 mm/min to 900 mm/min, the overall relative density decreases 0.1029%. In Figure 23, as laser power increases from 400 W to 700 W, the overall relative density increases 0.4495%. Visually comparing Figure 21 micrographs to Figure 23 values, it is evident laser power plays a huge role in reducing porosity and increasing relative density. Whereas increasing scan speed had little to minimal impact on 316H SS microstructure, suggesting scan speed is nearly independent of increasing or decreasing laser power. 316L SS studies on laser power nearly agree increasing laser power decreases porosity (Salmi et. al. 2024). Aversa reported increasing laser power resulted in lower porosity and denser material (Aversa, Marchese, and Bassini 2021). Kumaran et. al., 2021 found by increasing laser power from 400 W to 600 W, resulting in less porous, finer grain structures and higher microhardness value. However, there are conflicting results regarding the effect of scan speed on 316L SS porosity. Majumdar et al., 2005 observed as scan speed increased, porosity decreased (Majumdar et. al., 2005). Amar et. al., 2023 found scan speed did not affect porosity

in comparison to laser power (Kartikeya Sarma, Srinivas, and Kanmani Subbu 2021; Amar et. al., 2023). Several studies have shown low or high powder mass flow rate directly affects sample porosity (Amar et. al., 2023; Majumdar et. al., 2005; Lin et. al., 2020). Despite SS316H having higher carbon content, it did not greatly impact general trends in porosity, more so the microstructural phases because of DED. Because of the lack of studies in 316H SS process parameter and optimizations, further studies are required to see better trends in laser power, scan speed, hatch spacing, and porosity.

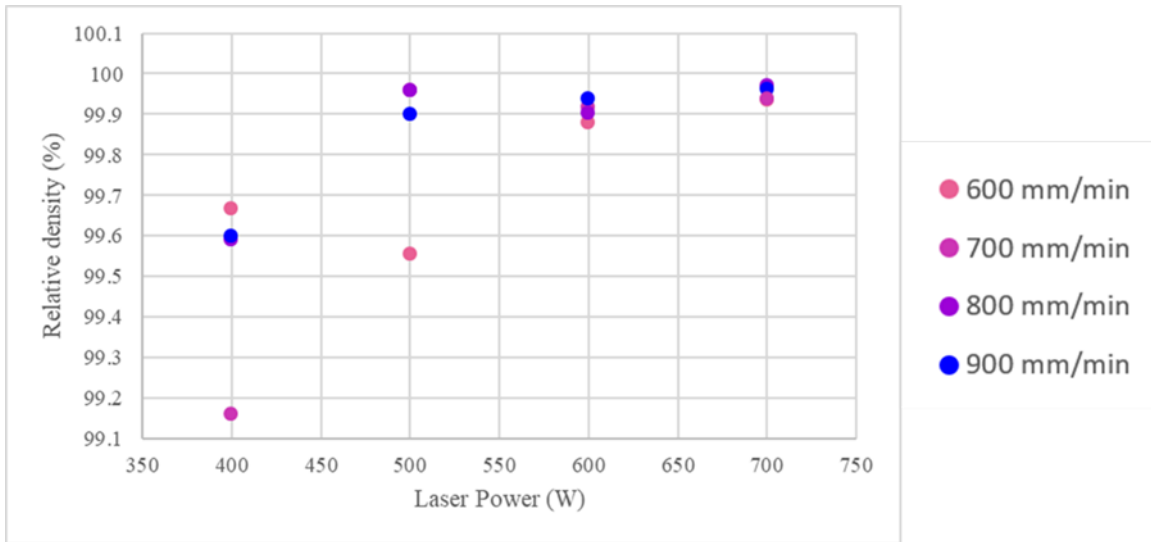


Figure 22. Effect of DED process parameters; laser power (W) at four different scan speeds (mm/min) on SS316H samples

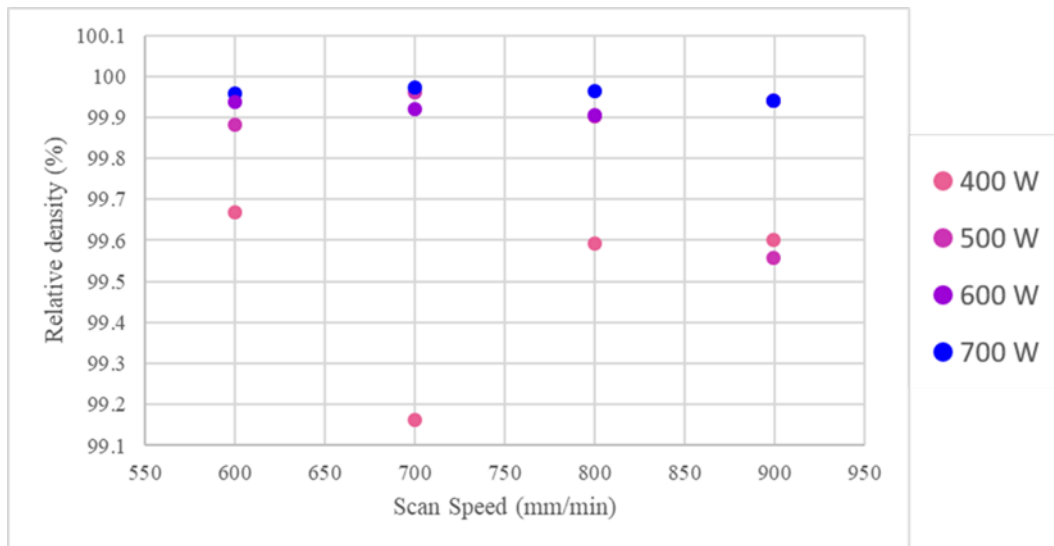


Figure 23. Effect of DED process parameters. Scan speed (mm/min) at four different laser powers (W) on 316H SS samples

4.0 Preliminary Results on 316L SS Cylindrical Samples

In this FY efforts, a modeling process was developed for the simulation of DED fabrication processes for residual stress predictions in a 316L cylinder of varying wall thickness. The simulated part was also fabricated experimentally using DED processes. In future works, this part is intended to serve as model validation. In this section, the effect of two different deposition paths were investigated for residual stresses and distortion in the part.

4.1 Experimentally Fabricated 316L Cylinder

This section introduces the DED experimentally fabricated 316L cylinder which is intended for future model validation. It is noted here that many details regarding the DED fabrication processes, and geometry are unknown to the authors, and thus many assumptions were made. Figure 24 (left) shows an available picture of the experimentally fabricated part, and Figure 24 (right) illustrates the assumed cross-sectional geometry with assumed/estimated dimensions. The cylinder is unique in that it has varying wall thickness, inner radius, and outer radius in the lower portion of the part. The upper portion of the part has constant wall thickness and inner and outer radius. The lower most inner and outer radius are assumed to be 49 mm and 60 mm, respectively. The inner and outer radius transition to a constant inner and outer radius at an assumed height of 20mm. The constant inner and outer radius are estimated as 64.62 mm and 67.02mm, respectively. The overall height is estimated to be 190 mm.

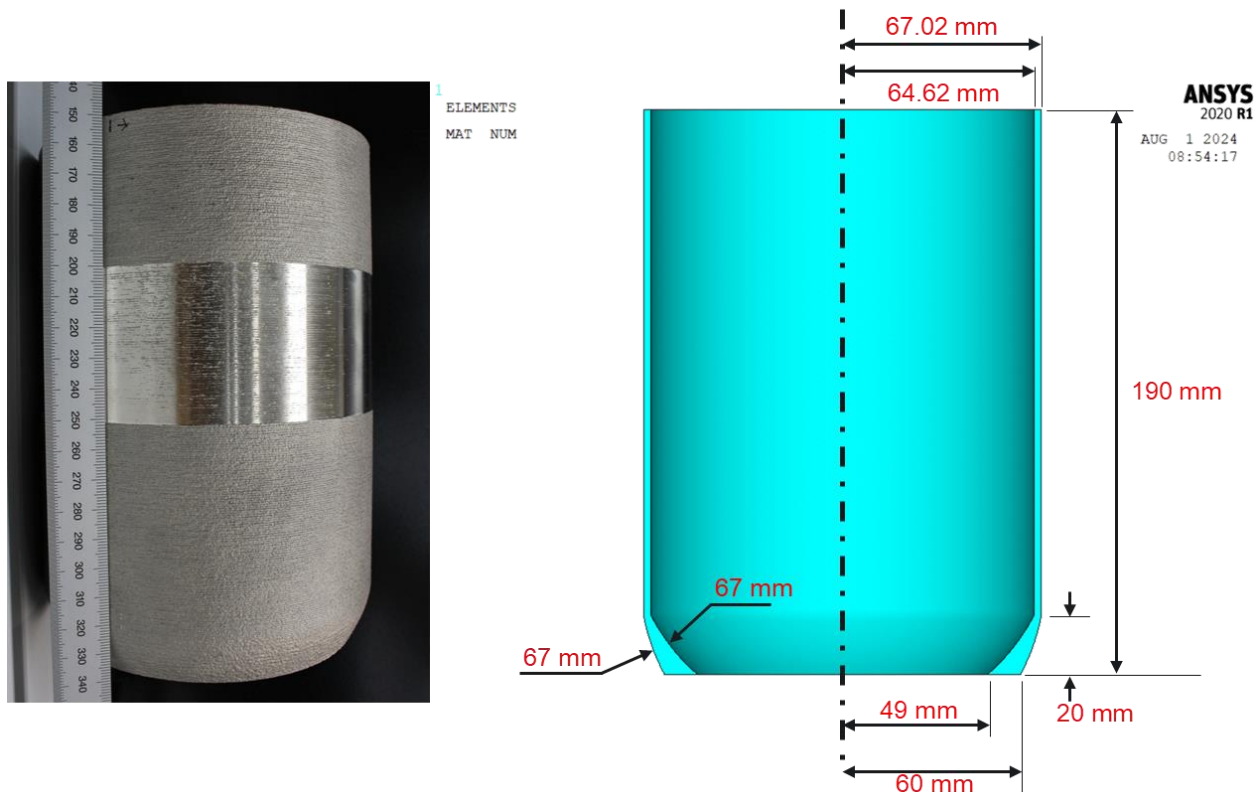


Figure 24. 316L SS cylinder geometry

The experimentally fabricated part was constructed using 234 through-height layers, beginning with the thick lower end of the part and progressing upward. All other DED fabrication process parameter information is not known to the authors. As such, simulation of the experimentally fabricated cylinder and its corresponding build process was not possible. Instead, a comparative study on the residual stress in the 316L cylinder was conducted using two different deposition paths and arbitrarily assumed fabrication process parameters (See Section 4.2.1.4).

4.2 Finite Element Modeling for DED Fabrication Processes

This section introduces the finite element modeling effort for DED fabrication processes. This work aims to develop a modeling methodology/framework for the simulation of transient temperature fields and corresponding macro residual stresses in microreactor parts fabricated through DED. The modeling process attempts to simulate the entire build process of the part as well as post-build cooling and baseplate removal. The simulation of such processes could provide valuable insight into the optimum build parameters to reduce residual stresses and distortion of the part prior to fabrication. These build parameters include deposition size, deposition speed, deposition pattern, ambient environment conditions, baseplate preheat conditions and other build specific thermal transient events.

4.2.1 Transient Thermal Model

This section introduces the transient thermal model used to predict the temperature fields from the building process of the 316L cylinder described in Section 4.1 using DED. The modeling approach is subdivided into two sequential analyses: a transient thermal analysis and a static structural analysis. The transient thermal analysis serves to predict the transient temperature fields from material deposition and post-build cooling. The static structural analysis (Section 4.2.2) is then used to predict the evolution of residual stresses from the transient temperature fields solved for in the transient thermal analysis. Both analyses were conducted using the commercial finite element software ANSYS 2020 R1. The remainder of this section will discuss the transient thermal model in detail. The geometry, loads and boundary conditions, contact conditions, and material properties is presented.

4.2.1.1 Geometry

The assumed geometry of the 316L cylinder is discussed previously in detail in Section 4.1. A cross-sectional view of the entire geometry is shown in Figure 25. Included in the geometry is a 25.4 mm thick baseplate. For computational efficiency, only a quarter of the 316L cylinder was simulated and discretized into 25 through-height layers. The discretization of the through-height build layers is coarse in comparison to the experimentally fabricated cylinder, which would correspond to approximately 59 layers for a quarter of the 316L cylinder. Future work is intended to validate that an approximate global stress behavior is accurately captured with this reduced number of simulated layers. This work is intended to provide the foundation that will provide insights to stress patterns early in the build process and help optimize and compare fabrication processes with reduced computational cost.

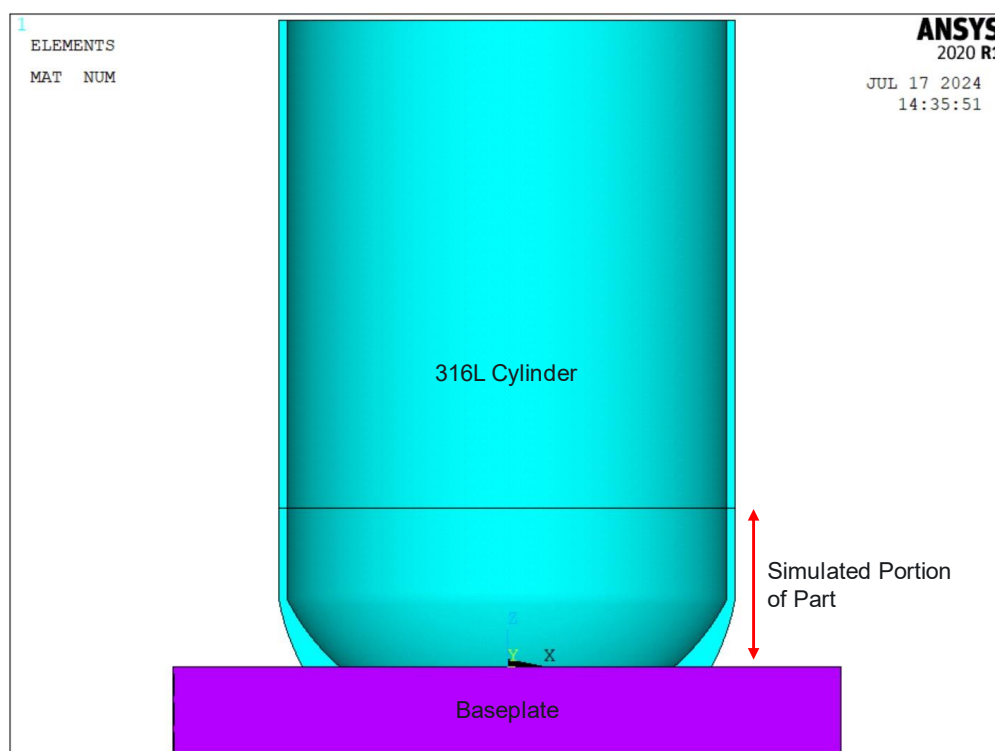


Figure 25. 316L SS cylinder finite element model geometry

4.2.1.2 Material Properties

Temperature dependent thermal material properties for 316L were implemented in the analyses. The cylinder and baseplate are assumed to share the same material properties. A tabulated list of the thermal material properties is given in Table 6.

Table 6. 316L SS thermal material properties (Kim, 1975)

Temperature (K)	Thermal Conductivity $\frac{W}{m \cdot K}$	Heat Capacity $\frac{J}{kg \cdot K}$	Density $\frac{kg}{m^3}$
300	13.96	498.97	7,954.00
400	15.53	512.37	7,910.00
500	17.10	525.76	7,864.00
600	18.68	538.74	7,818.00
700	20.25	552.13	7,771.00
800	21.82	565.53	7,723.00
900	23.39	578.92	7,674.00
1,000	24.96	591.90	7,624.00
1,100	26.53	605.30	7,574.00
1,200	28.10	618.69	7,523.00
1,300	29.67	632.09	7,471.00
1,400	31.25	645.06	7,419.00
1,500	32.82	658.46	7,365.00
1,600	34.39	671.85	7,311.00
1,700	35.96	685.25	7,256.00

4.2.1.3 Element Types

The 3D solid elements that comprise the 316L cylinder and baseplate were generated using SOLID278 elements. Default element key options were used for the SOLID278 elements.

The thermal contact between the 316L cylinder and baseplate was employed using CONTA174 elements on the bottom of the 316L cylinder and TARGE170 elements on the top of the baseplate. The convection on the top of each through-height layer was employed using SURF154 elements overlayed on the top of each through-height layer.

4.2.1.4 Loads and Boundary Conditions

The build process of the part is simulated using the element birth and death technique and the geometry of the part is subdivided into a series of deposition segments that are activated according to the deposition path of interest. Both a circumferential and raster style deposition path are independently simulated and compared. An equivalent mesh and deposition segment size was used for both studies, and only the deposition path was altered. In the circumferential style build, the wall thickness of each through-height layer is subdivided into two through-thickness layers which define the deposition path along the circumference. The inner most layer is deposited first, followed by the outer most layer. In the raster style build, an alternating deposition path that radially follows the through-wall thickness of the part is employed. Analogous to the circumferential style build, the raster style build contains two through-thickness segments for each pass. The deposition paths of the circumferential and raster style build on a quarter view of the model are shown in Figure 26.

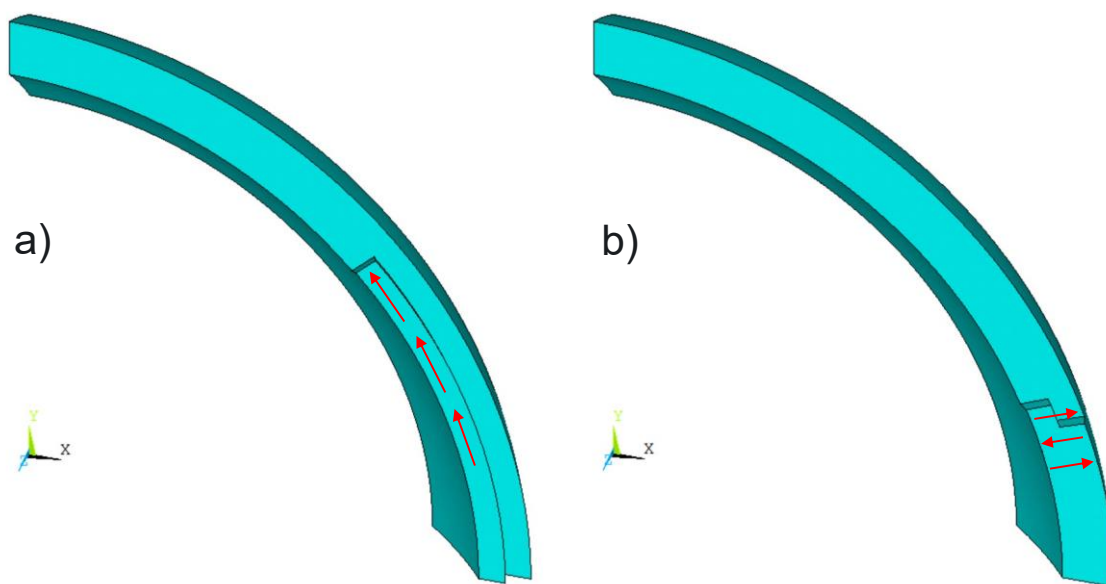


Figure 26. Deposition paths. Circumferential style (a) and raster style (b)

The deposition segments for both deposition paths were activated according to a deposition speed of 2 cm/s. Once activated, the elements were held at melt temperature (1375 °C) for a duration of time that corresponds to the speed, direction, and size of the segment in order to mimic the advancing melt pool.

In the circumferential style build, the deposition time for each segment was approximated as the arc length of the segment divided by the deposition speed. In the raster style build, the

deposition time for each segment was approximated as the linear radial length of the segment divided by the deposition speed. When the deposition time for a segment completes, the melt temperature boundary condition is released, and the segment is allowed to cool according to the ambient environment and adjacent material.

The ambient environment was assumed to be air at 25 °C with a film coefficient equal to $10 \frac{W}{m^2 K}$. Convection boundary conditions were applied to the interior and exterior edges of the cylinder via nodal loads, as well as to the top of each through-height layer via convection elements. The convection boundary conditions become active once the material is deposited. The convection boundary condition is then deactivated once a subsequent layer is deposited onto the active layer.

Heat transfer between the part and the baseplate is achieved through thermal contact elements and a thermal contact conductance which is assumed to be perfectly conductive. The entire baseplate is prescribed an 80 °C initial temperature condition at the beginning of the analyses, and the bottom of the baseplate was prescribed a constant pre-heat temperature of 80 °C. The bottom of the baseplate preheat temperature remains constant for the entire analysis. Convection boundary conditions, equivalent to those described above, were applied to the top of the baseplate (excluding the region where the cylinder is bonded to the baseplate) via nodal loads. No convection boundary conditions were applied on the outer edges of the baseplate. After the build process is completed, the part is allowed to cool for a duration of 2 hours.

4.2.2 Static Structural Model

This section introduces the static structural model used to predict the residual stress field and part distortion from the building process of the 316L cylinder using DED. The static structural model receives the temperature fields from the transient thermal model as inputs during the simulated build process. The geometry, loads and boundary conditions, contact conditions, and material properties is discussed in detail.

4.2.2.1 Geometry

The geometry and mesh for the static structural model is equivalent to the transient thermal model (Section 4.2.1.1). Only a quarter of the build was simulated in the static structural model.

4.2.2.2 Material Properties

Temperature dependent mechanical material properties for 316L were employed in the analyses. The baseplate was simulated using a purely linear elastic material model. The cylinder was simulated as an elastic-plastic material which employed the Von-Mises isotropic hardening material model. Temperature dependent bilinear hardening curves were employed for the plasticity model. A tabulated list of the mechanical material properties is given in Table 7 (Nickel Institute, 2020, Sandmeyer Steel Company, 2014). No extrapolation is made for materials beyond the reported temperatures.

Table 7. 316L SS mechanical material properties (Nickel Institute, 2020, Sandmeyer Steel Company, 2014)

Temperature (K)	Youngs Modulus (GPa)	Yield Strength (MPa)	Hardening Slope (MPa)	Mean Coefficient of Thermal Expansion (cm/cm/°C)	Poisson Ratio
300.15	193	290	579.74	16.6	0.25
422.15	190	201	597.42	16.80	-
533.15	181	172	676.82	17.24	-
644.15	172	159	726.96	17.68	-
755.15	162	148	716.29	18.13	-
866.15	153	140	710.57	18.42	-
977.15	143	131	498.74	18.69	-
1089.2	132	110	181.31	18.96	-
1,273.15	-	-	-	19.40	-

4.2.2.3 Element Types

The 3D solid elements that comprise the 316L cylinder and baseplate were generated using SOLID185 elements. Default element key options were used for the SOLID185 elements.

The bonded contact between the 316L cylinder and baseplate was employed using CONTA174 elements on the bottom of the 316L cylinder and TARGE170 elements on the top of the baseplate.

4.2.2.4 Loads and Boundary Conditions

The simulated build process for the static structural model is equivalent to the transient thermal model. The build process is simulated by activating a series of deposition segments according to the deposition path. However, special care is necessary to ensure that the activated segments are activated in a thermal strain-free condition. To achieve this, the temperatures at the end of each activation step are imported and solved for first, followed by the activation of the intended segment in the following load step. This ensures that the activated segment and adjacent edges of material are at the melt temperature during activation, providing a thermal strain-free condition. Thermal stresses are then generated from temperature changes in the material after activation and corresponding thermal expansion/contraction.

The baseplate was prescribed a thermal strain-free temperature of 25 °C and was fixed in the out-of-plane direction along its bottom surface. Additional minimum boundary conditions were prescribed to the bottom surface of the baseplate to prevent rigid body translation/rotation. Bonded contact was employed to handle the contact between the part and baseplate.

The structural solution was obtained for all activation segments and corresponding temperature fields during the build process of the solution. A total of 20 equally space time solutions were obtained for the cool down phase. An additional load step is implemented to ensure that the part and baseplate are brought to a uniform 25 °C. Lastly, the baseplate is removed to achieve the final state of the fabricated part. Minimum boundary conditions were applied to the bottom of the part to prevent rigid body translation/rotation after the baseplate was removed.

Both the circumferential style and raster style deposition paths for the quarter part build were studied in the static structural model. Gravity was ignored.

4.2.3 Finite Element Model Results

This section presents the simulated results for the quarter height DED manufactured 316L cylinder using two different build path strategies: circumferential style build and raster style build. The simulated time for the build process of the geometry was 0.55 hours and 0.22 hours for the circumferential style build and raster style build, respectively. Figure 27 displays the layer-wise mean temperature in the part as a function of layer height. The first 25 fabrication steps correspond to the complete deposition of each layer in the fabrication process. As such, the mean temperature was calculated at the completion time for each layer. The fabrication steps beyond step 25 correspond to the cool down of the completed part. It is observed that larger through-height temperature gradients and higher temperatures exist at layer completion in the raster style build compared to the circumferential style build. This could be explained by the shorter build time required in the raster style build, decreasing the time for heat transfer to occur to the ambient environment. Figure 28 shows an isometric view of the temperature field at completion of deposition (fabrication step 25). A relatively uniform temperature is observed for each layer along the circumference of the part, aside from the topmost layers.

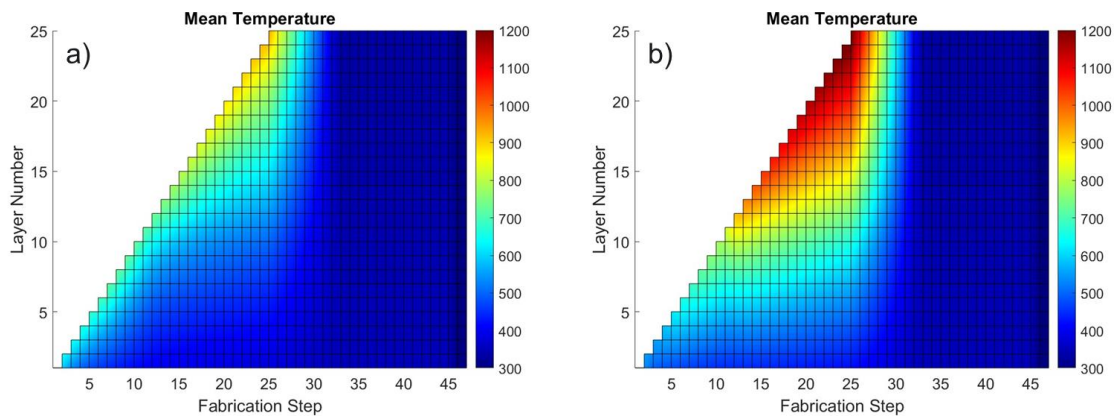


Figure 27. Layer-wise mean temperature (K). Circumferential style build (a) and raster style build (b)

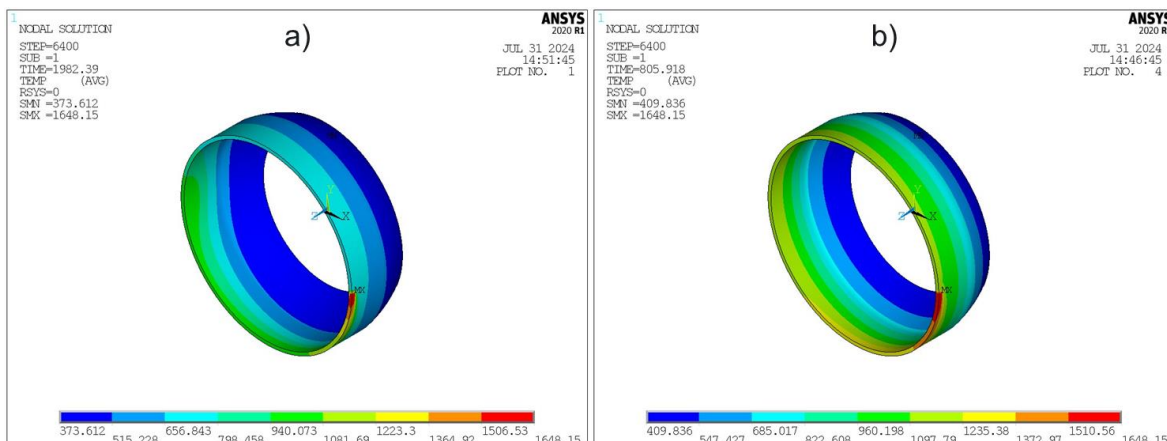


Figure 28. Part temperature (K) at completion of build (fabrication step 25). Circumferential style build (a) and raster style build (b).

The layer-wise hoop stress was monitored during the fabrication process given the thin wall nature of the part. To determine if stress gradients exist through the wall thickness, the layer-wise average hoop stress at the inner wall, outer wall, and total layer were calculated for each through-height layer. Figure 29, Figure 30, and Figure 31 illustrate the mean hoop stress field for each layer during the fabrication process at the inner wall, outer wall, and total layer, respectively. The first 25 fabrication steps correspond to the complete deposition of each layer in the fabrication process. As such, the mean stress fields were calculated at the completion time for each layer. The fabrication steps beyond step 25 correspond to the cool down of the completed part. The final step corresponds to the baseplate removal.

The overall global stress behavior between the circumferential and raster style builds are similar, with varying magnitude. During the deposition and subsequent cooling, through-height hoop stress gradients are present with higher tensile behavior in the lower portion of the build, followed by reduced tensile behavior in the upper portion of the build. The topmost layers experience elevated uniform tensile dominant behavior. The presence of through thickness hoop stress gradients are evident with increased tensile behavior occurring on the outer wall of the part compared to the inner wall, with the maximum stress occurring in the lower portion of the part after cooling, prior to baseplate removal. At the last fabrication step (baseplate removal), both the circumferential style and raster style build paths experience a large reduction in the tensile stress state in the lower portion of the part, indicating a new equilibrium state from the release of the baseplate.

It is observed, however, that the circumferential style build experiences more compressive behavior in the upper, inner-wall of the part compared to the raster style build. Further, less tensile behavior is experienced in the lower, inner-wall in the raster style build compared the circumferential style build. Lastly, the raster style build experience less tensile behavior in the topmost layers compared to the circumferential style build. These differences suggests that different deposition paths could be employed at varying portions of the build to reduce the residual stress field during fabrication.

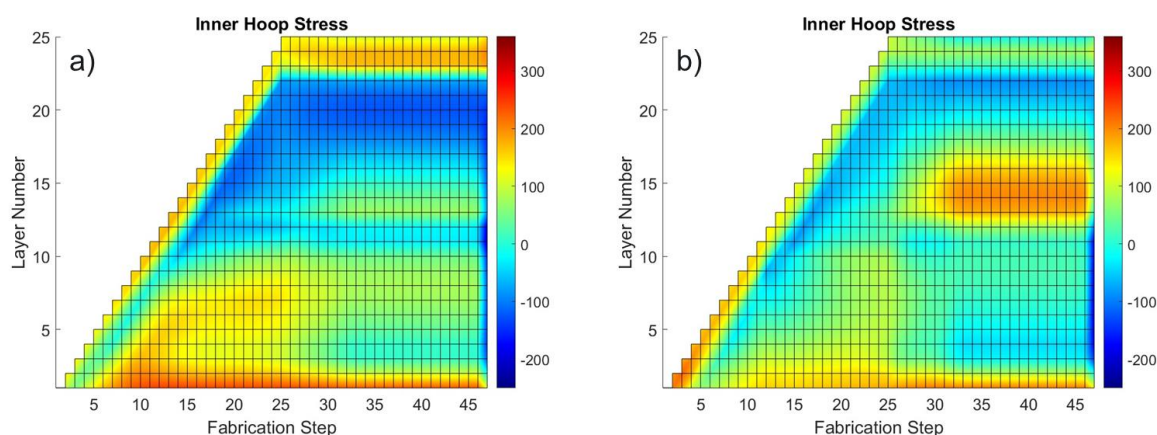


Figure 29. Layer-wise inner hoop stress (MPa). Circumferential style build (a) and raster style build (b).

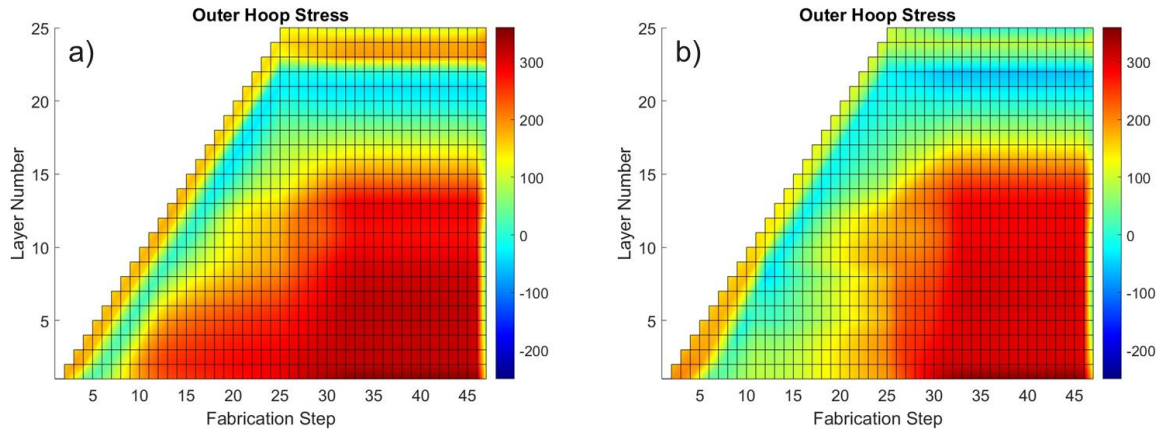


Figure 30. Layer-wise outer hoop stress (MPa). Circumferential style build (a) and raster style build (b)

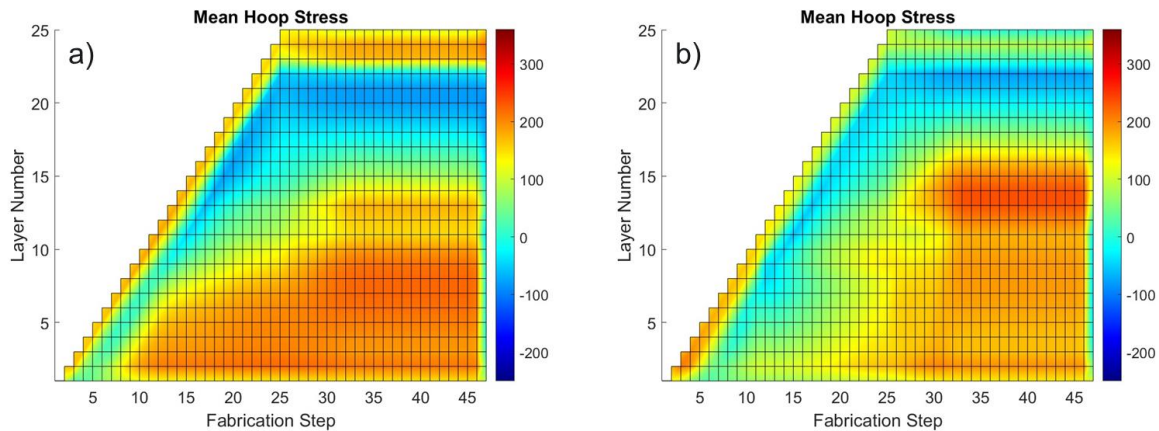


Figure 31. Layer-wise total hoop stress (MPa). Circumferential style build (a) and raster style build (b).

Contours of the hoop stress in the part at the completion of build (fabrication step 25), post cooling pre-baseplate removal, and post cooling post-baseplate removal are shown in Figure 32, Figure 33, and Figure 34, respectively. The stress behavior through the height of the part for all three states follow the same trends previously discussed. It is observed however, that the hoop stress is more uniform circumferentially in the raster style build compared to the circumferential style build in all three stress states.

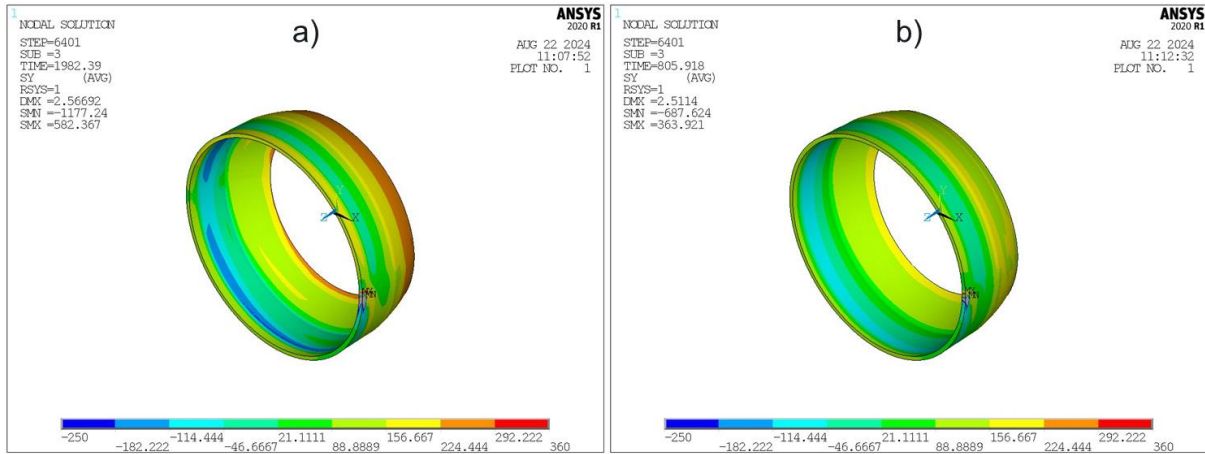


Figure 32. Part hoop stress (MPa) at completion of build (fabrication step 25). Circumferential style build (a) and raster style build (b)

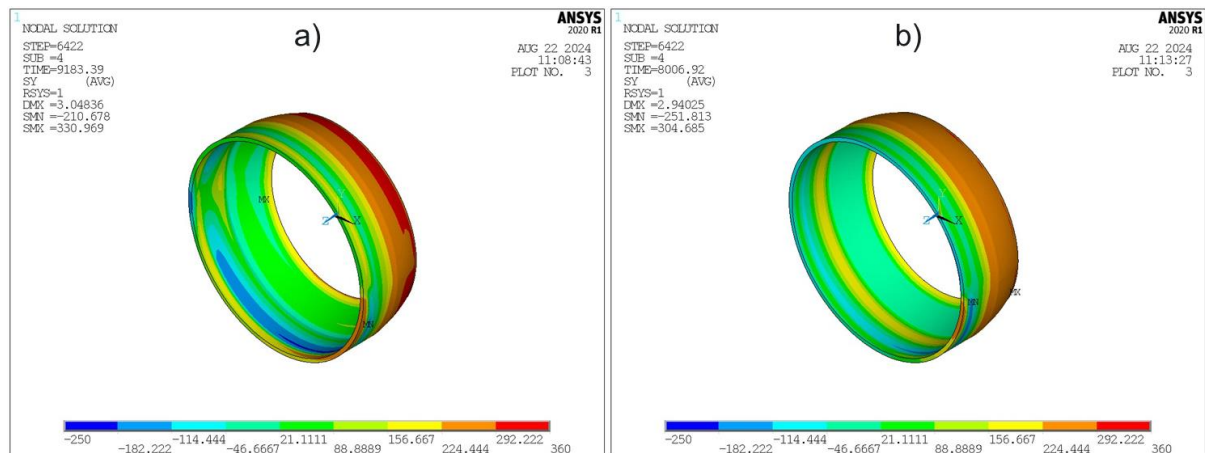


Figure 33. Part hoop stress (MPa) at post-cooling, pre-baseplate removal. Circumferential style build (a) and raster style build (b)

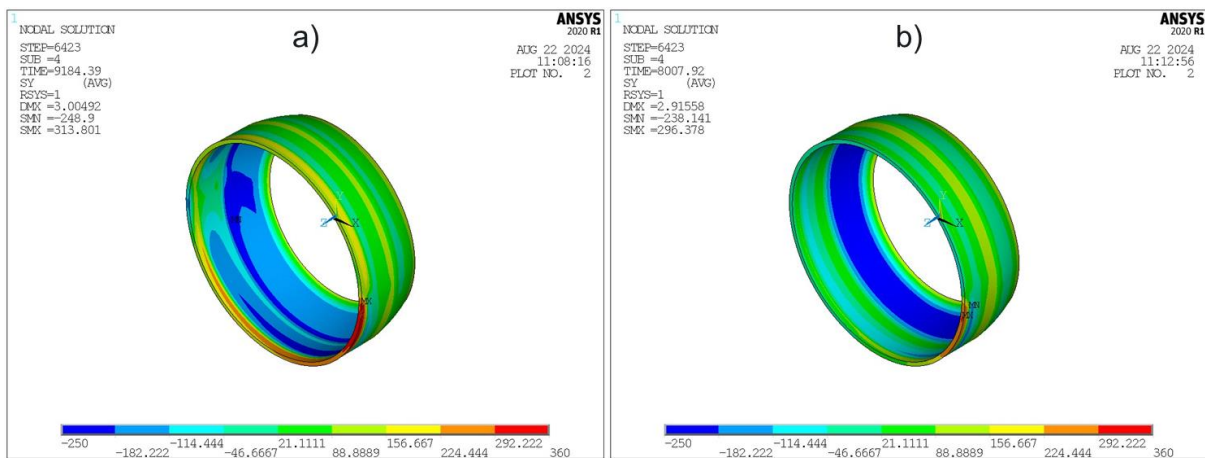


Figure 34. Part hoop stress (MPa) at post-cooling, post-baseplate removal. Circumferential style build (a) and raster style build (b)

The effect of baseplate removal is shown in Figure 35, Figure 36, and Figure 37, which display the layer-wise average hoop stress at the inner wall, outer wall, and total layer for pre and post baseplate removal after post build cooling, respectively. The location of zero stress on the horizontal axis is indicated by a green dotted vertical line. As previously discussed, both the circumferential and raster style builds experience a reduction in the tensile stress state in the lower, outer wall of the part after baseplate removal. The lower, inner wall is driven into compression. This shift in the stress state can be explained by the rigid/welded connection between the bottom of the part and the baseplate, which constrains the part from equilibrium prior to baseplate removal. The upper portion of the part experiences less change in the stress field due to increased distance from the point of constraint.

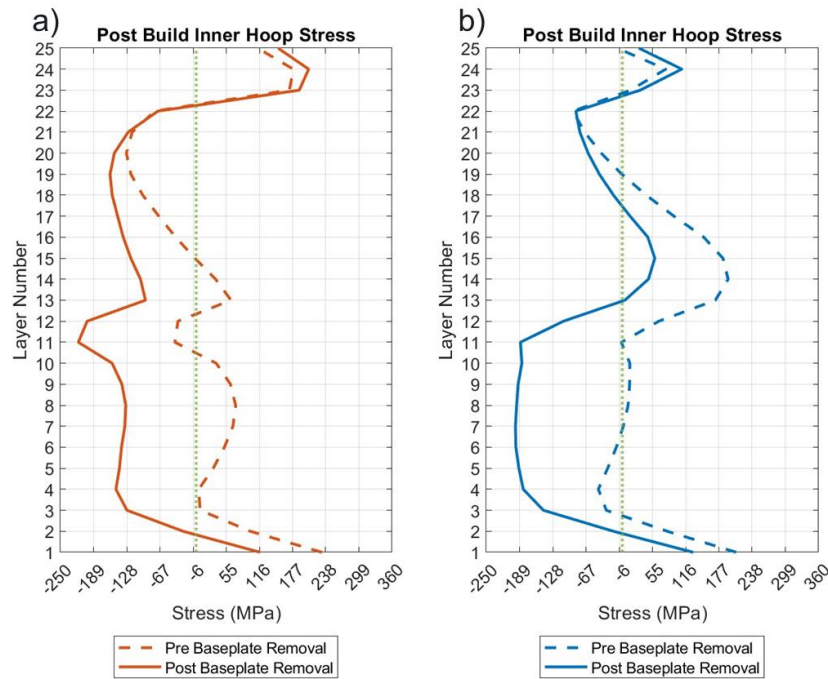


Figure 35. Post-cooling layer-wise inner hoop stress. Circumferential style build (a) and raster style build (b).

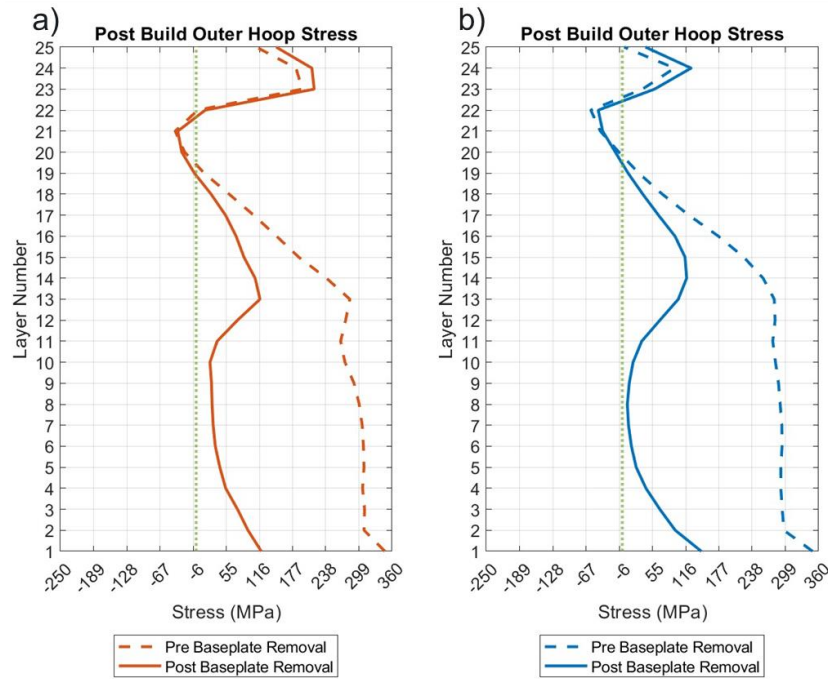


Figure 36. Post-cooling layer-wise outer hoop stress. Circumferential style build (a) and raster style build (b).

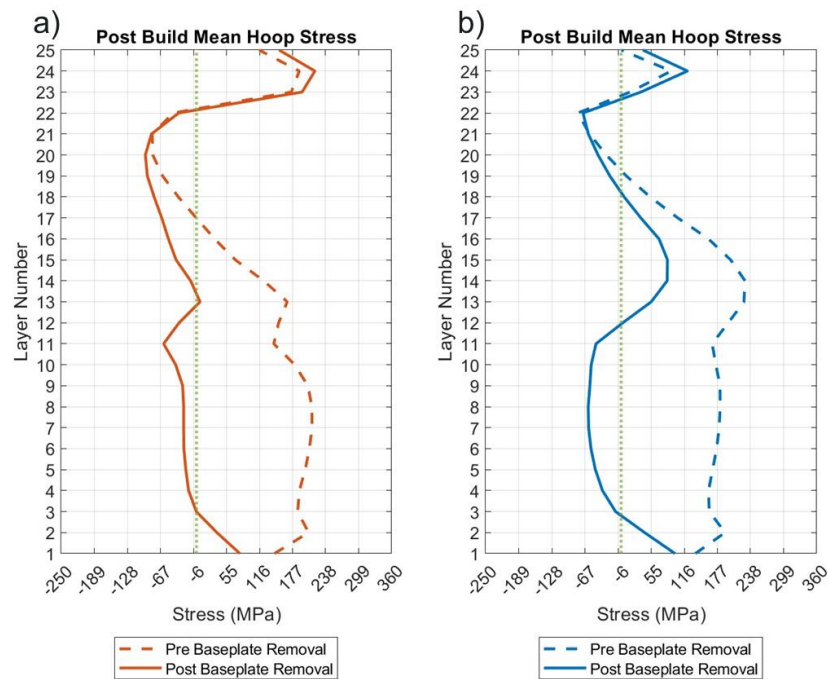


Figure 37. Post-cooling layer-wise total hoop stress. Circumferential style build (a) and raster style build (b).

The comparative final stress states, both pre and post baseplate removal, are shown on the same axes in Figure 38. The location of zero stress on the horizontal axis is indicated by a green dotted vertical line. After baseplate removal, the raster style build exhibits higher compressive residual stress than the circumferential style build for the first 10 layers. For layers 10-22 the inverse is true, with larger compressive stresses being observed for the circumferential style build. For layers 23-25, the raster style build exhibits reduced tensile stresses. These differences in the final stress states at different layers further suggest that different deposition paths could be employed at varying portions of the build to reduce the residual stress field during fabrication.

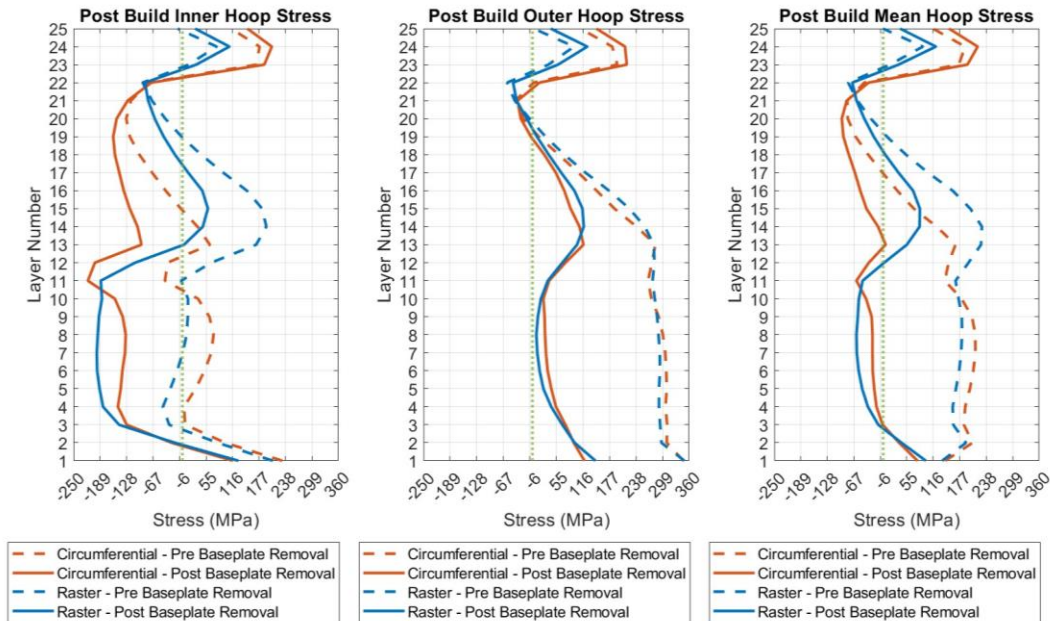


Figure 38. Post-cooling comparative hoop stress

An exaggerated final deformed shape of the DED manufactured 316L cylinder after baseplate removal is displayed in Figure 39 and Figure 40 which show a side profile and top view of the part. The deformations in these graphics are amplified by 6x the actual deformation. These figures show that potentially significant differences in deformation can be observed when different deposition paths are used during the build process. When the deformations are critical during the part build, this kind of analysis can help direct the build parameters and deposition paths to create the desired final product.

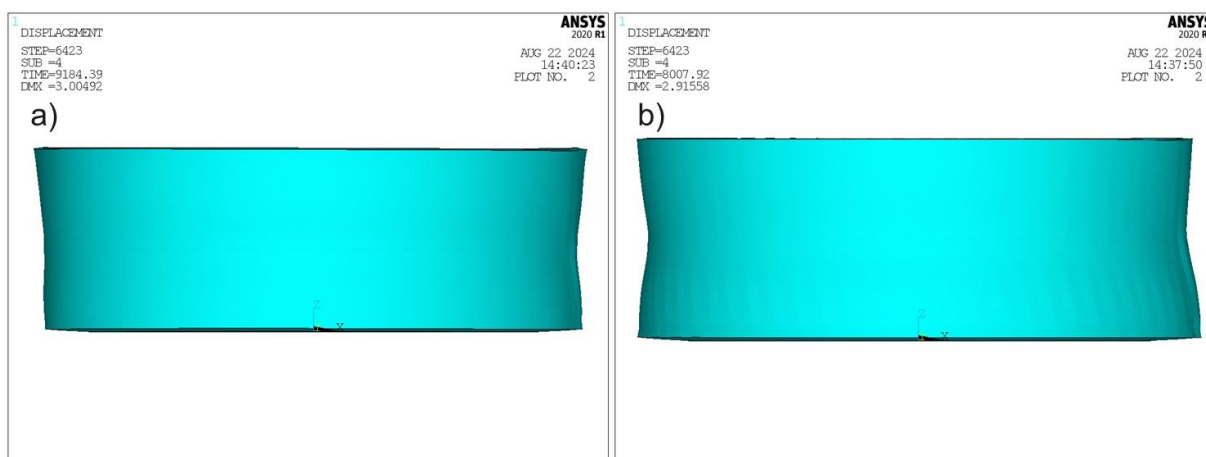


Figure 39. Deformed shape magnified 6x, side profile view. Circumferential style build (a) and raster style build (b)

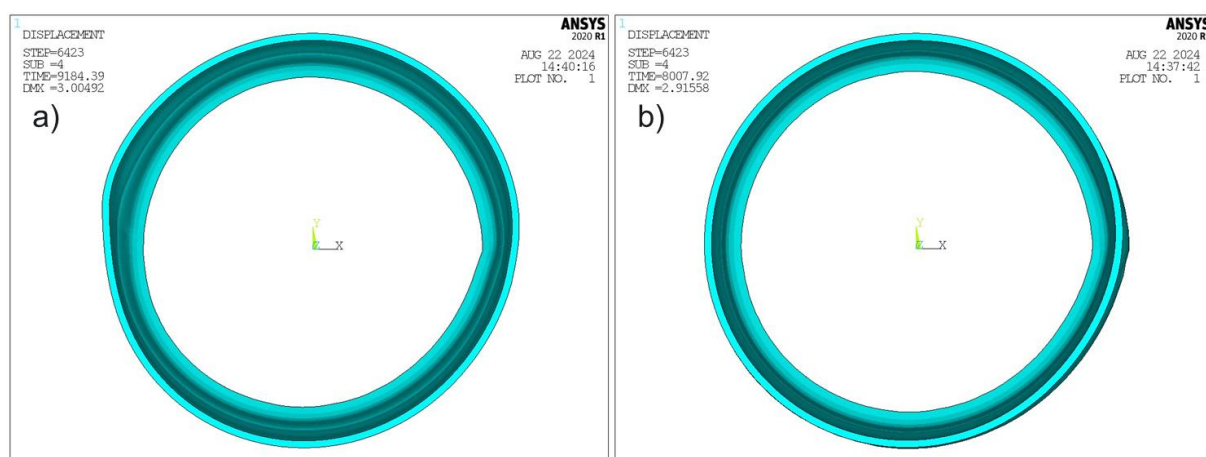


Figure 40. Deformed shape magnified 6x, top view. Circumferential style build (a) and raster style build (b).

4.3 SS316L SS Cylinder: Evaluation and Characterization

The 316L SS DED built cylinder was evaluated using NDE and electron microscopic analysis to understand defect, microstructural features. The XRD measurements for structural and residual stress analysis is planned in future.

4.3.1 NDE Summary

The development and use of post-process NDE methods is essential to the qualification and verification of materials and components from AM processes such as LPBF and DED. The objectives of applying and developing NDE methods applicable to AM components are to identify the presence of porosity and internal defects, characterize the microstructure, assess the mechanical properties, and measure geometric conformity in the post-build condition. Combined with the in-situ monitoring data obtained during the build process, the use of post-process NDE will be able to further demonstrate the component conformance to material and geometric requirements. Overcoming the challenges of the unique characteristics of AM

components and materials (e.g. surface roughness, geometric complexity, microstructural features, and defect morphology) to provide reliable and high resolution NDE is recognized as a critical element to qualifying these components for safety critical applications.

The NDE approach to assess the condition of the DED 316L pipe component utilized a frequency analysis of the reflected ultrasonic amplitude spectrum to measure the wall thickness variations throughout the component. Due to the complex nature of the surface conditions of the DED 316L pipe component, traditional pulse-echo methods experience large signal loss and low signal-to-noise ratios (S/N) leading to other considerations for component inspections. The objective of this effort is to assess the ability of the reflected ultrasonic amplitude spectrum frequency analysis method to account for the surface roughness conditions and allow for wall thickness and defect evaluations to be performed.

The method to measure the geometric wall thickness uses a continuous wave ultrasonic signal to generate reflected signals that contain information on the reflectance and transmittance characteristics of the component. At certain frequencies (resonance frequencies), these reflected waves exhibit a reduction in amplitude that correspond to multiples of the wall thickness. Using an estimate of the speed of sound in the material, the wall thickness can be calculated from the frequencies corresponding to the amplitude reductions in the reflectance.

The large surface roughness features caused by the powder DED fabrication process will complicate the reflectance and transmittance of ultrasonic wave signals from the component. To evaluate the impact of the surface features, mechanical removal of the ridges was performed using a lathe on both the inside and outside surface. Four (4) zones were created along the axial height of the component corresponding to inside smooth – outside rough, inside smooth – outside smooth, inside rough – outside smooth, and finally inside rough – outside rough (as-manufactured). Each of the machined regions are approximately 25 mm in length along the axial height. In addition, a Dremel tool was used to score the inside surface within the smooth-smooth region to provide a simulated surface defect.

The DED 316L cylinder component was placed in a scanner setup specifically constructed to perform ultrasonic scans in a cylindrical geometry. The scanner device was originally designed to perform inner surface scans of reactor vessel head penetrations in both the circumferential and axial directions. For application to the DED 316L cylinder component, a fixture was developed to fit over the bottom end of the pipe component with the ultrasonic transducer positioned adjacent to the outer surface. The cylinder and transducer were submerged in water and the scans were performed from the top of the cylinder and extending approximately 170 mm along the axial length. About 20 mm of the component residing in the fixturing was not scanned. A picture of the scanner setup is shown in Figure 41.

A 10 MHz broadband transducer with a 0.75 in spot size and a 4-inch focal length was used to generate a continuous sinusoidal wave ultrasonic signal. The reflected ultrasonic wave was received at the transducer and the data collected for post-processing. Using Fast Fourier Transform (FFT) methods, resonance frequencies were obtained at each measurement location. Scanning was performed at 0.5-degree increments in the azimuthal direction and 0.1 mm axial increments. This approach allowed for a detailed map of the component wall thickness to be obtained and generated graphically.

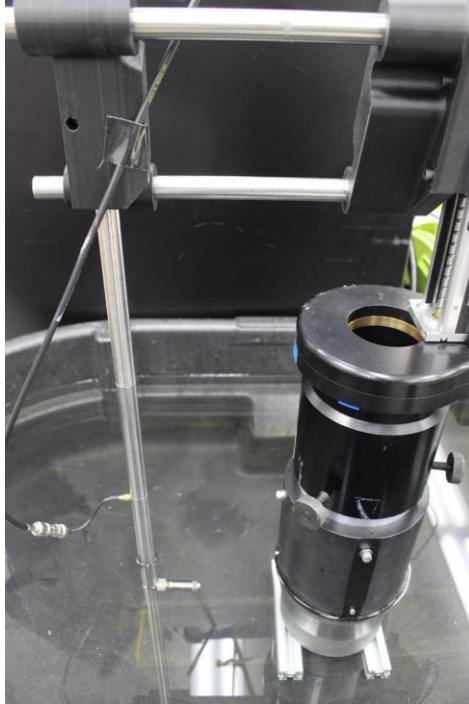


Figure 41. Scanner and transducer setup for NDE of the DED 316L component

The data obtained from the outer surface ultrasonic scan was post-processed using a Python script to obtain the resonance frequencies using FFT analysis. The data was separated into two groups of resonances that provided information on the wall thickness. An averaging method was applied to generate the wall thickness results shown in Figure 42.

The wall thickness measurements using the ultrasonic NDE method observes all four of the regions of the component; rough inside surface – rough outside surface, smooth inside surface – rough outside surface, smooth inside surface – smooth outside surface, and rough inside surface – smooth outside surface. The as-manufactured wall thickness is shown to vary between 2.0 mm and 2.3 mm. Some local values outside this range are observed and could be an indication of signal noise or local variations due to the roughness. Variations in the wall thickness are observed in the regions that surface roughness was machined off. This could be an indication that the component contained some ovality that caused uneven machining to occur. This ovality appears to have a maximum at the 180 degree location. However, some variation in the ovality along the length can be seen in the results. The wall thickness measurements in the machined zones exhibits more uniformity as compared to the as-manufactured regions

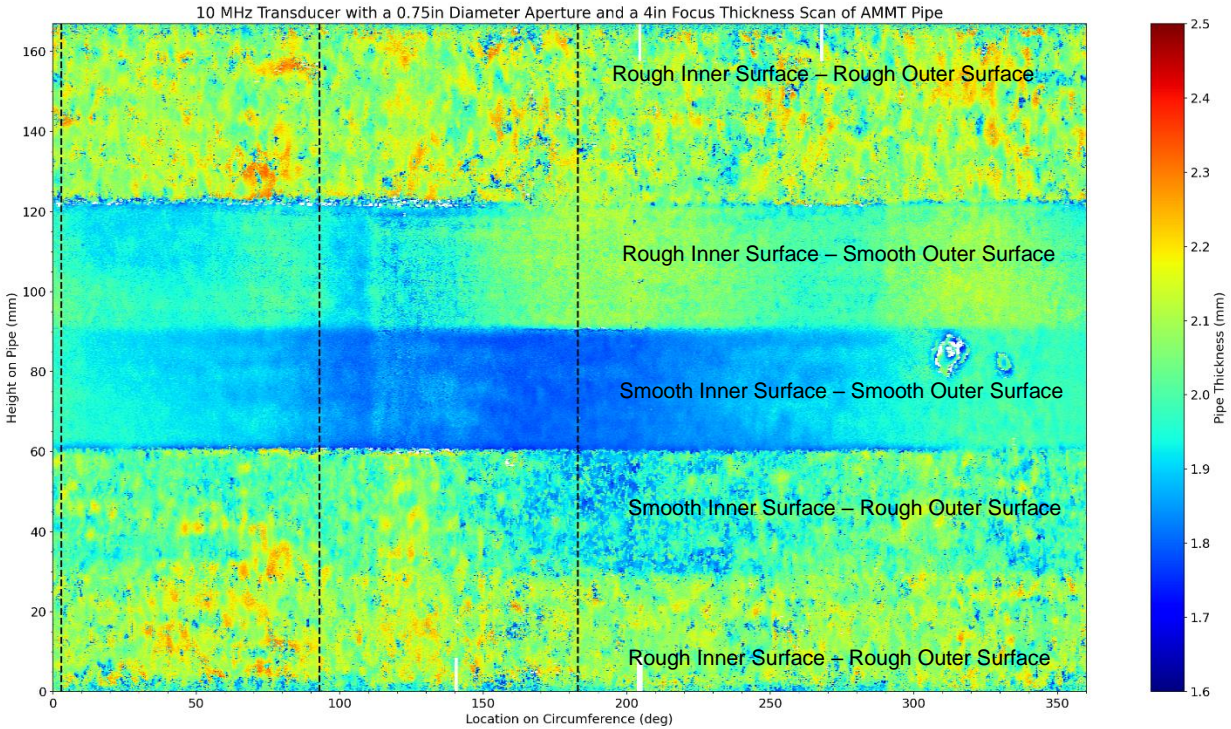


Figure 42. DED 316L SS component wall thickness contour map from the ultrasonic NDE measurements. Machined surface zones are indicated by text. Locations for wall thickness measurements using destructive methods are indicate by a vertical dashed line.

Upon completion of the NDE wall thickness measurements, a destructive examination plan was developed to obtain wall thickness measurements, perform metallographic examines of the microstructure, and residual stress measurements. An initial sectioning plan is shown in Figure 43 and Figure 44. The component was sectioned into four (4) 90-degree pieces and a 4 mm wide strip was removed at 0°, 90°, 180°, and 270° for further examinations.

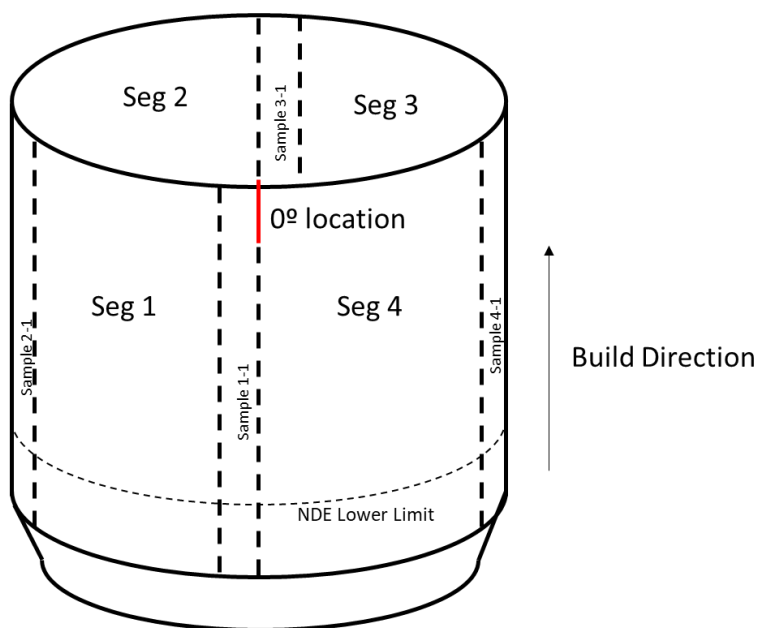


Figure 43. Sectioning plan for the DED 316L SS component.

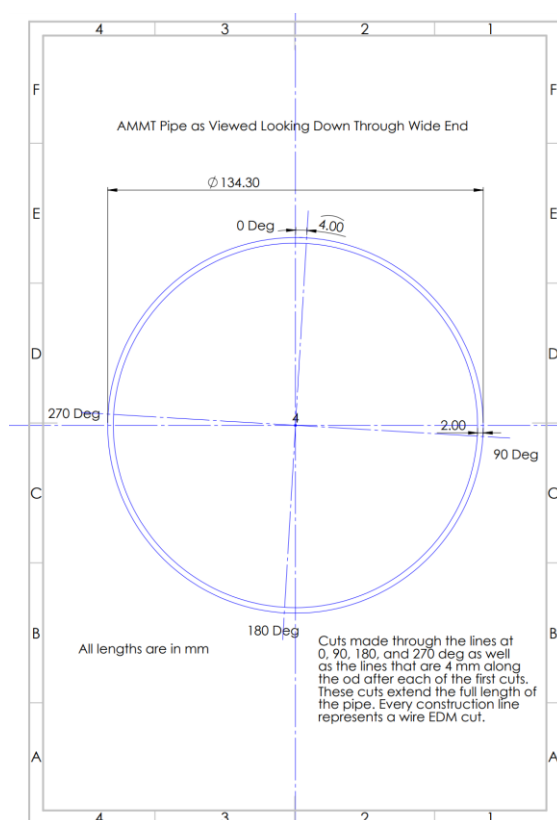


Figure 44. Cross-section view of the sectioning plan showing the 4 mm wide specimens cut from the DED 316 L SS component.

Three of the 4 mm wide specimens were examined using an optical method to obtain the wall thickness variation along the axial length of the component. Results for the optical wall thickness measurement at the 0° location is shown in Figure 45 along with comparison to the values obtained from the NDE ultrasonic method. Good agreement is seen between the wall thickness measurements obtained from the destructive optical technique and the NDE method. The impact of the surface roughness on both destructive and destructive measurements is observed in the figure. Based on these measurements, the surface roughness is on the order of 0.1 to 0.2 mm.

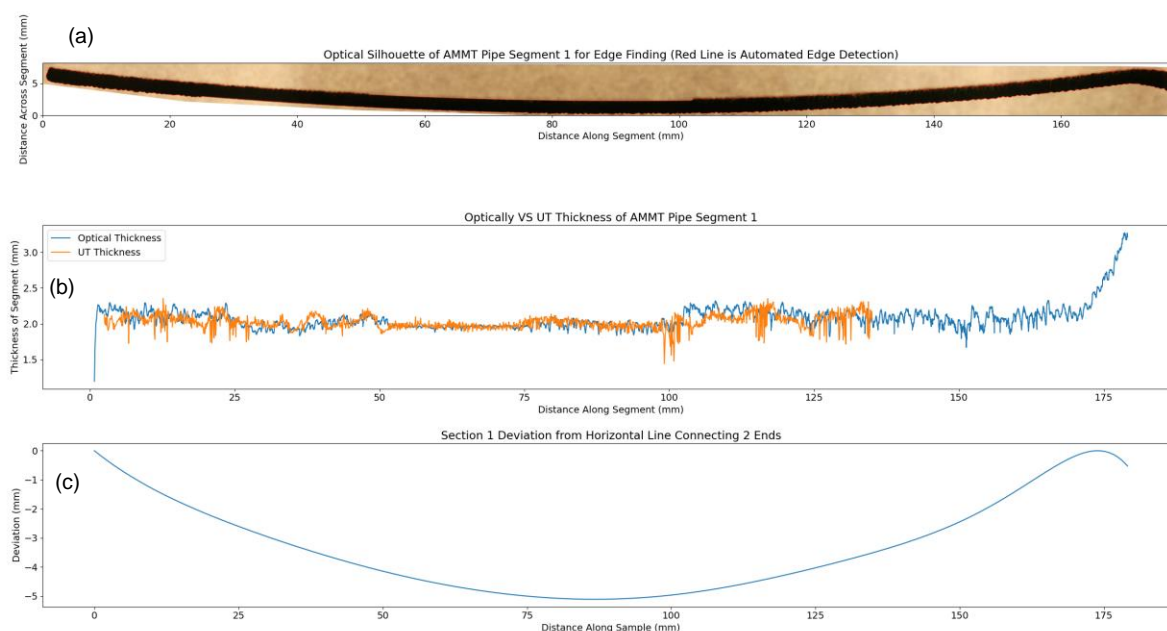


Figure 45. Results for the optical wall thickness measurement at the 0° location. (a) Optical silhouette of the 4 mm wide strip section from the 0° location. (b) comparison of the NDE and optical wall thickness measurements and (c) amount of deflection from perfect straightness.

4.3.2 Metallurgical Analysis

The 4 mm wide strip sectioned from the 270° location was further sectioned near the top and bottom of the 175 mm long piece for examination using SEM to gain an understanding of the microstructure of the 316L component produced using powder DED. The process of rapid melting and cooling is expected to produce a unique and complicated microstructure within the wall thickness of the component.

The Thermo Fisher FEI Quanta focused ion beam (FIB) Scanning Electron Microscope was used for the backscattered electron imaging to reveal the microstructure of the DED processed 316L component. The SEM backscattered images obtained from the topmost region from the 270° section is presented in Figure 46. The low mag SEM image in Figure 46(a) reveals the presence of long-columnar and fine-equiaxed grains in the as-printed microstructure. While the equiaxed grains are strictly confined to the edges of the thin wall, the columnar grains are found extending into the center (along the thickness) and eventually arching towards the top following the build direction. The high mag image of the center region of the wall in Figure 46(b) shows the columnar grains curving towards the top. The bimodal nature observed in the grain

morphology can be explained by the differences in the cooling rates between the center and the edges of the thin wall. The edges experience a significantly higher cooling rates compared to the center. The higher cooling rates produce higher undercooling below the melting point enhancing the nucleation rate of the solid particles within the liquid melt. The higher nucleation rate finally leads to the formation of equiaxed microstructures (Liu et.al., 2019).

The medium and high mag SEM backscattered images from the left and right edges of the thin wall are presented in Figure 46(c,d) and Figure 46(e,f), respectively. Although the size of the equiaxed grains seemed to be the same between the left and right edges, there appears to be a slight difference in the depth of the equiaxed grain regions. The left edge exhibited equiaxed grains up to a depth of ~192 microns from the edge while the right edge had equiaxed only up to ~164 microns. Besides, the as printed microstructures also exhibited solidification cells formed due to the DED processing as shown in Figure (g,h). The lighter contrast in the solidification cell walls in Figure 46(h) could likely be due to the segregation of elements with higher atomic number such as Mo. Energy-Dispersive Spectroscopy (EDS) mapping would be necessary to confirm the same.

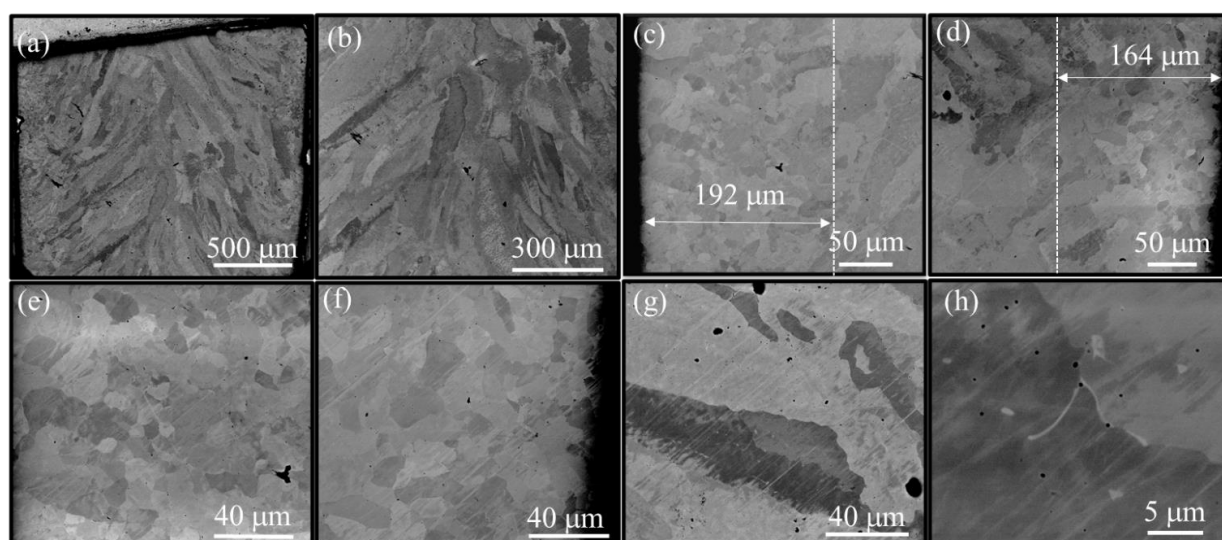


Figure 46. SEM backscattered images obtained from the topmost region of a longitudinally cut specimen of the DED processed 316L SS cylinder.

The SEM backscattered montage image of part of the bottom region removed from the 270° specimen is presented in Figure 47. The bottom also exhibited the curved columnar grains like the top section. However, the bottom section is substantially wider than the top section hence the presence of multiple tracks from the laser deposition can be noticed in the montage image. Furthermore, the high magnification imaging performed on the bottom region revealed solidification cells identical to the top section. Hence EDS mapping was performed to characterize the solidification cells and the resultant elemental maps are presented in Figure 48. The anticipated enrichment of Mo in the solidification cell walls can be clearly observed in Figure 48(d). Besides, these cell walls are also found to be lean in iron and slightly enriched in chromium.

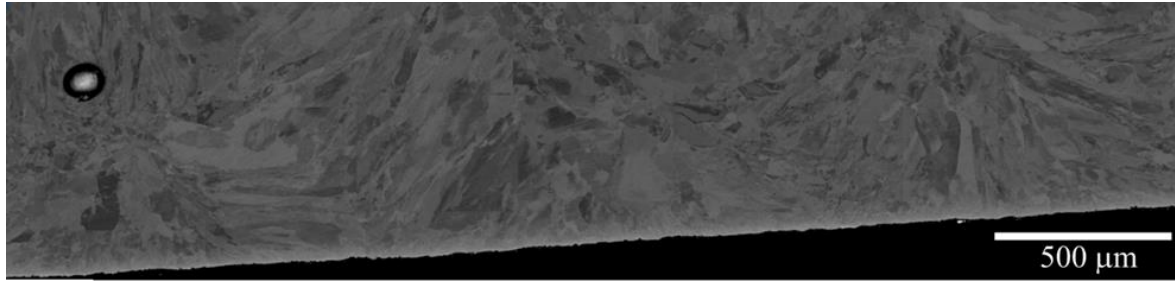


Figure 47. SEM backscattered montage image obtained from the bottom-most region of a longitudinally cut specimen of the DED processed 316L SS component

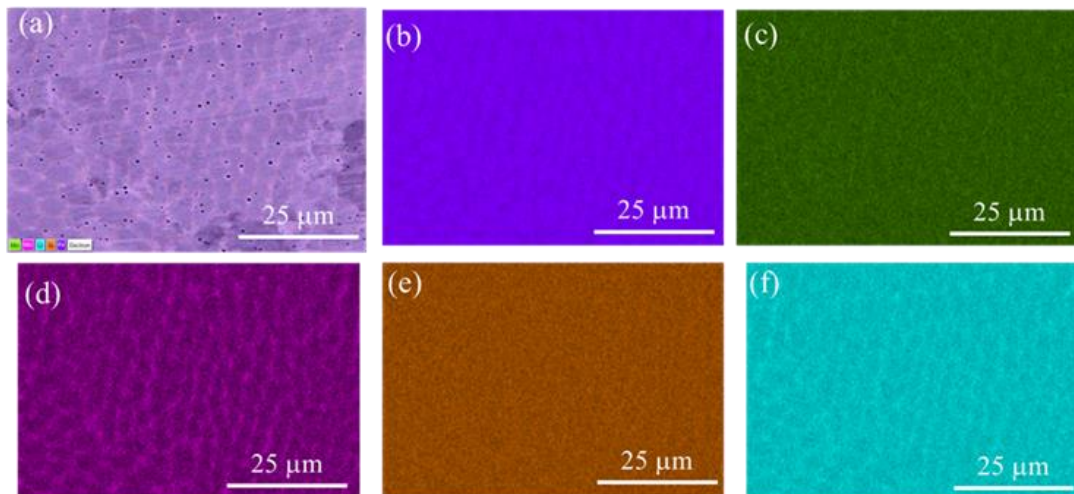


Figure 48. SEM backscattered montage image of part of the bottom region removed from the 270° specimen. (a) EDS layered image of the solidification cells. Elemental maps of (b) iron, (c) manganese, (d) molybdenum, (e) nickel, and (f) chromium.

5.0 Full Scale 316L SS Microreactor Heat Exchange Liner: Preliminary Results

As mentioned earlier, as part of a feasibility study, the Marvel program requested an additive manufactured heat exchanger liner from 316H, due to the time sensitivity of the project, demonstration using 316L was also supported. A full-scale liner was produced by RPMi using DED with 316L powders with a -140/+325 mesh size and 1070W. This manufacturing work was performed under AMMT work package CR-22PN040202 (Activity CR-22PN0402025). Measurements are in inches. Because the part was produced using DED, some dimensions had to be changed compared to the requested dimensions. The wall thickness for example was increased from 0.063 to 0.085 in and the thickness of the base and funnel had to be increased to avoid warpage of the part during the build. Figure 49 shows the liner build in progress at layers 951 and 1202 respectively and the completed DED liner removed from the baseplate is shown in Figure 50. The wall thickness comparison post deposition averaged $\pm 0.010/-0.006$ (Standard Deviation(in): 0.010) based on the 3D model based on nominal 0.088 minimum wall thickness is shown in Figure 51. (Comparison based on model "RPMi Modified_Liner for Complete Machining 1_stp" provided to PNNL on November 29, 2023). No machining or metallurgical examination was funded although this liner full scale build is currently be used as a typical full scale Additive component for the NDE demonstration and will be reported elsewhere.

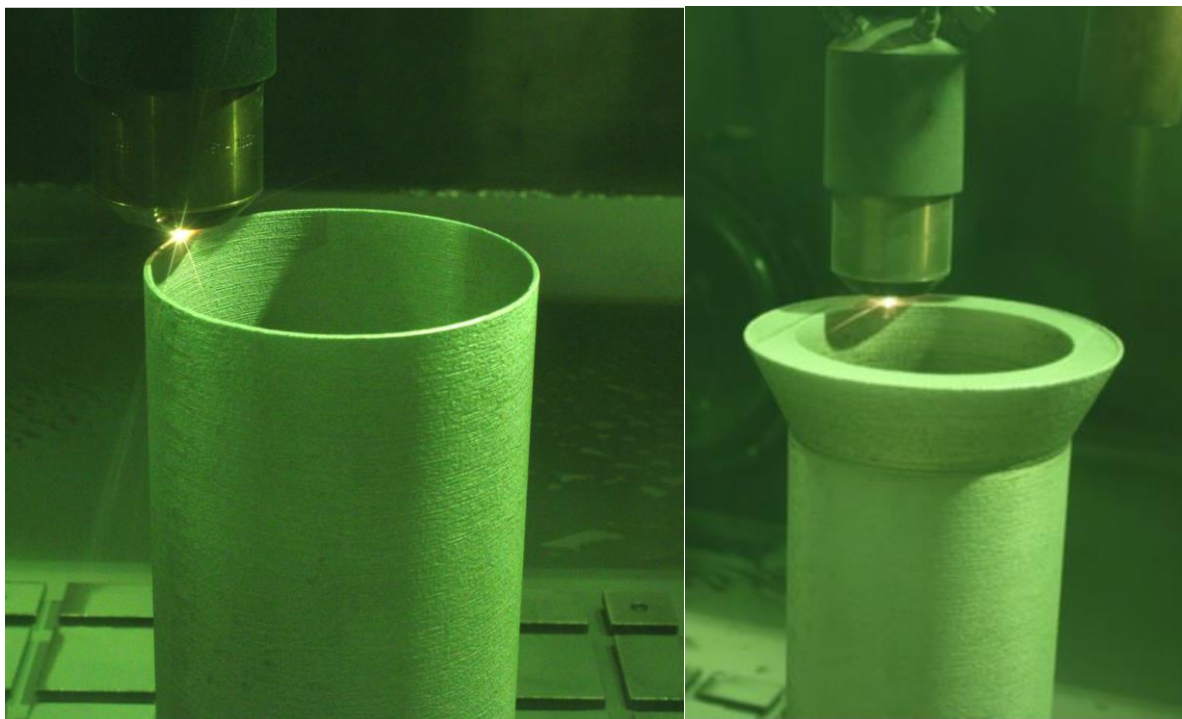


Figure 49. Liner built in progress at layer 951 and layer 1202, respectively



Figure 50. Completed DED liner removed from the baseplate

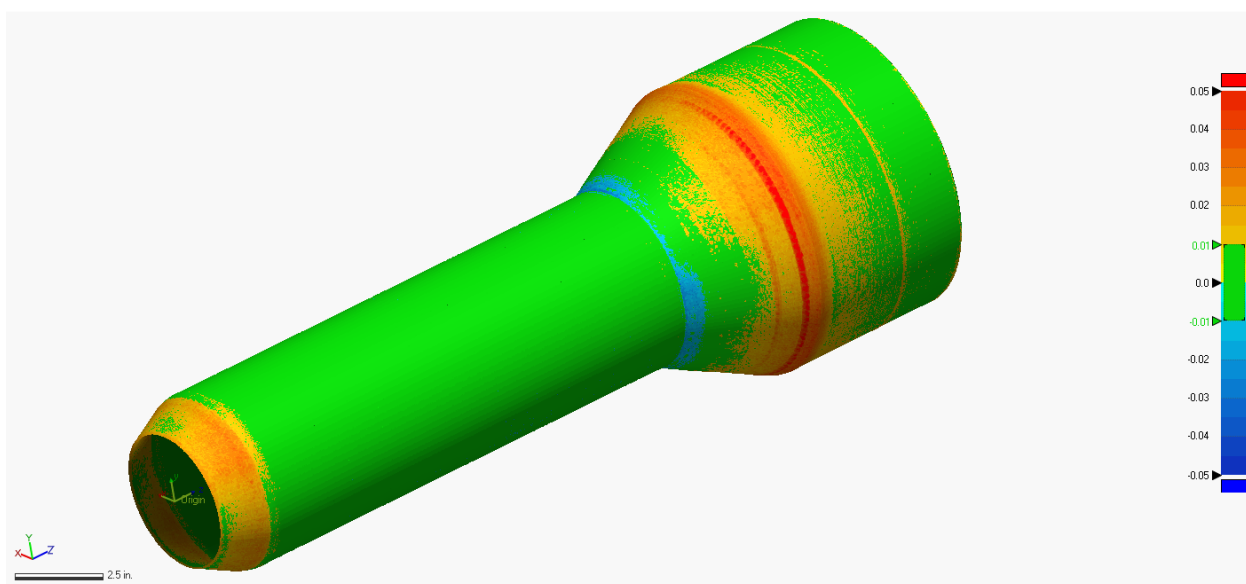


Figure 51. Dimensional measurements and comparison post deposition. (3D model based on nominal 0.088 minimum wall thickness. Comparison based on model "RPMI Modified_Liner for Complete Machining 1_stp" provided to PNNL on November 29, 2023)

6.0 Summary and Future Work

A benchmark study was developed that included design, development, manufacturing, and performance measurement of agnostic reactor relevant geometries to support industry's adoption of AM in a variety of structures. A matrix of five microreactor component geometries, specifically based on the recent feasibility study on a Marvel microreactor liner, was developed and the PNNL team initiated one material/process combination, namely 316H SS using laser powder DED. Although the benchmark starts initially with simplistic cubical and cylindrical forms, it builds up to a mock-up of a non-proprietary design, that can demonstrate a variety of features that can be useful to present knowledge to specific designers of microreactors and also for other reactor type designers. The initial cubical and cylindrical forms are steps to obtain surface features and dimensional responses to the identified process parameters to be used in the non-proprietary design mockup.

The powder DED technique has been identified as the technique for the FY 2024 benchmark study due to multiple reasons, namely:

- leverage cylindrical sample pieces manufactured during the development stages of the full-scale DED 316L liner
- increased industry interest
- minimize overlap with the large investment in LPBF project scope of the AMMT program
- provide information to decrease the gap in knowledge and data for codes and standards
- interest from the international GIF community potential for complex parts with unique options to minimize weldments
- prevent overlap with the GIF Material board research projects that is currently been finalized.

By performing the benchmark study, the AMMT program will therefore provide nuclear energy stakeholders with another manufacturing option and knowledge to apply for accelerated readiness for new or replacement designs, therefore accelerates demonstration.

This project proposes using an expanded pipe that leads into an elbow. This component is extremely difficult and costly to manufacture through traditional methods, and it also can reduce space needed for traditional transition areas. This design allows for a smooth transition from a larger pipe to a smaller pipe at the location of a 90° bend and has potential to increase fluid flow and reduce turbulence. Thus, the expanded elbow pipe is an excellent candidate for demonstrating the ability to use DED for manufacturing of microreactor components.

Although only limited characterization was completed, the main findings are described below:

1. *316H SS cubical samples*: A 316H SS powder DED literature survey and a parameter confirmation study on 16 cubical samples were performed for power levels of 400–700 W and scan speeds ranged from 600–900 mm/min. We found that the quality (based on porosity content) is independent of scan speed for a laser power of 700 W. However, at lower laser power, it seems that the lower scan speed yields larger porosity levels and more size defects. These parameters are being used for the printing of the cylindrical samples currently in process.

2. *316L cylindrical sample*: The evaluation of the cylinder from 316L SS yielded good agreement between the wall thickness measurements obtained from the destructive optical technique and the NDE method. The impact of the surface roughness on both destructive and destructive measurements was observed and needs to be explored further for full application and resolution. Based on these measurements, the surface roughness is on the order of 0.1–0.2 mm. Although metallurgical examination of the 316L SS cylinder sample is not completed, we noted that the cellular structure is similar between samples from the top and bottom. Segregation is noted in these cellular cells as the cell walls are iron-lean and slightly chromium-rich. We recommend that this observation be compared with results from other studies.

The finite element modeling and analysis effort that was performed to understand the temperature field, residual stresses, and deformation present at the conclusion of the DED build process for a 316L SS cylinder. The assumed build parameters were a deposition speed of 2 cm/s, a material melt temperature of 1,375 °C, a bottom surface baseplate temperature held at 80°C, 2 hours of cooldown time, and an ambient environmental temperature and film coefficient of 25°C and $10 \frac{W}{m^2K}$, respectively. Two deposition paths were described and modeled: 1) circumferential style and 2) raster style. At this time, these build parameters are assumed because the actual build parameters used in the fabrication of the cylinder were not available at the time of publishing the work. The finite element model was used in both a thermal and structural analysis, with the thermal analysis performed before the structural analysis. The thermal analysis provided the temperature field of the component during the build process and the 2-hour cooldown after the build. The structural analysis used the time-history temperature field data to determine the residual stresses and deformations in the cylinder during the build, cooldown period, and baseplate removal.

1. Results from the finite element analyses were presented for both deposition paths. The differences between the temperature fields, residual stresses, and cylinder deformations in each are presented and described. Notably, this process of using the FEA to determine the resulting temperatures, stresses, and deformations could be used in future analyses to determine optimal build paths during future DED fabrication efforts.
2. The next steps for this work will be to implement build parameters that accurately represent the experimentally fabricated cylinder. Once these parameters have been obtained, a representative FEA study can be conducted. The 316L SS cylinder that was fabricated using DED can undergo examination to determine the residual stresses present in the physical part. These stresses then can be compared to the FEA results to determine the accuracy of the model and for further refinement as necessary. Additionally, future modeling efforts could include modeling alternate materials such as a 316H SS cylinder with the same geometry presented in this work.
3. Additional To improve this modeling effort, a mesh refinement study should be conducted to determine the optimal mesh density for the cylinder. This includes determining the adequate number of layers vertically along the cylinder axis and radially through the cylinder wall thickness that provide enough detail to ensure accuracy.
4. Finally, future work exploring finite element modeling of potential DED components to be used in microreactors, such as expanded elbow pipes, expanded straight pipes, two-axis pipes, flanged elbows without expansion, heat exchangers, pumps, and valves, should be performed.

In conclusion, the geometry benchmark matrix with associated characterization matrix forms a good basis for continuation for the 316H SS/DED combination which can be expanded to a 316H SS/LPBF combination to evaluate the different effects if these two processes are used, and also to leverage the parameter optimization work performed under other AMMT program projects.

7.0 References

- Amar, E., V. Popov, V. M. Sharma, S. Andreev Batat, D. Halperin, and N. Eliaz. 2023. "Response Surface Methodology (RSM) Approach for Optimizing the Processing Parameters of 316L SS in Directed Energy Deposition." *Materials (Basel)* 16 (23). <https://doi.org/10.3390/ma16237253>. <https://www.ncbi.nlm.nih.gov/pubmed/38067997>.
- ANSYS 2020 R1, ANSYS Inc., Southpointe 2600 ANSYS Drive, Canonsburg, Pennsylvania.
- Aversa, Alberta, Giulio Marchese, and Emilio Bassini. 2021. "Directed Energy Deposition of AISI 316L Stainless Steel Powder: Effect of Process Parameters." *Metals* 11 (6). <https://doi.org/10.3390/met11060932>.
- Bartlett, J. L., & Li, X. (2019). An overview of residual stresses in metal powder bed fusion. *Additive Manufacturing*, 27, 131-149. <https://doi.org/10.1016/j.addma.2019.02.020>
- Bartlett, J. L., Croom, B. P., Burdick, J., Henkel, D., & Li, X. (2018). Revealing mechanisms of residual stress development in additive manufacturing via digital image correlation. *Additive Manufacturing*, 22, 1-12. <https://doi.org/10.1016/j.addma.2018.04.025>
- Bobzin, K., Wietheger, W., Knoch, M. A., Schacht, A., Reisgen, U., Sharma, R., & Oster, L. (2020). Comparison of Residual Stress Measurements Conducted by X-ray Stress Analysis and Incremental Hole Drilling Method. *Journal of Thermal Spray Technology*, 29(6), 1218-1228. <https://doi.org/10.1007/s11666-020-01056-z>
- Boruah, D., Dewagtere, N., Ahmad, B., Nunes, R., Tacq, J., Zhang, X., Guo, H., Verlinde, W., & De Waele, W. (2023). Digital Image Correlation for Measuring Full-Field Residual Stresses in Wire and Arc Additive Manufactured Components. *Materials (Basel)*, 16(4). <https://doi.org/10.3390/ma16041702>
- Chen, S.-g., Gao, H.-j., Zhang, Y.-d., Wu, Q., Gao, Z.-h., & Zhou, X. (2022). Review on residual stresses in metal additive manufacturing: formation mechanisms, parameter dependencies, prediction and control approaches. *Journal of Materials Research and Technology*, 17, 2950-2974. <https://doi.org/10.1016/j.jmrt.2022.02.054>
- Dai, H., Francis, J. A., Stone, H. J., Bhadeshia, H. K. D. H., & Withers, P. J. (2008). Characterizing Phase Transformations and Their Effects on Ferritic Weld Residual Stresses with X-Rays and Neutrons. *Metallurgical and Materials Transactions A*, 39(13), 3070-3078. <https://doi.org/10.1007/s11661-008-9616-0>
- DeNonno, Olivia, Juan Felipe Gonzales, Stephen Tate, Robert Hamlin, and Jonah Klemm-Toole. 2024. "Role of Austenite Stability in Elevated Temperature Mechanical Properties of Gas Metal Arc-Directed Energy Deposition Austenitic Stainless Steels." *Jom* 76 (5): 2268-2282. <https://doi.org/10.1007/s11837-024-06489-3>.
- Ding, D., Huang, R., Liu, T., Yuan, L., & Liu, C. (2023). Effects of path patterns on residual stresses and deformations of directed energy deposition-arc built blocks. *Virtual and Physical Prototyping*, 19(1). <https://doi.org/10.1080/17452759.2023.2296128>

Doniger, William, Cody Falconer, Adrien Couet, and Kumar Sridharan. 2023. "Corrosion of 316L & 316H stainless steel in molten LiF-NaF-KF (FLiNaK)." *Journal of Nuclear Materials* 579. <https://doi.org/10.1016/j.jnucmat.2023.154383>.

Goel, S., Neikter, M., Capek, J., Polatidis, E., Colliander, M. H., Joshi, S., & Pederson, R. (2020). Residual stress determination by neutron diffraction in powder bed fusion-built Alloy 718: Influence of process parameters and post-treatment. *Materials & Design*, 195. <https://doi.org/10.1016/j.matdes.2020.109045>

Gonzalez, Juan, Stephen Tate, and Jonah Klemm-Toole. 2023. "Microstructure and Mechanical Property Stability of Wire Arc Directed Energy Deposition Austenitic Stainless Steels During Thermal Aging at 650°C." *Jom* 75 (11): 4793-4807. <https://doi.org/10.1007/s11837-023-06120-x>.

Gradl, P. 2022. *Journal of materials Engineering and Performance*, 31:6013-6044.

Hares, E. A., M. Mostafavi, R. Bradford, and C. E. Truman. 2018. "The effect of creep strain rate on damage accumulation in Type 316H austenitic stainless steel." *International Journal of Pressure Vessels and Piping* 168: 132-141. <https://doi.org/10.1016/j.ijpvp.2018.09.015>.

Hartmann, T., S. Maloy, M. Komarasamy, "Materials scorecards, Phase 2," PNNL-32744, PNNL, March 2022.

Herzog, Dirk, Vanessa Seyda, Eric Wycisk, and Claus Emmelmann. 2016. "Additive manufacturing of metals." *Acta Materialia* 117: 371-392. <https://doi.org/10.1016/j.actamat.2016.07.019>.

Huan, H., Liu, L., Mandelis, A., Peng, C., Chen, X., & Zhan, J. (2020). Mechanical Strength Evaluation of Elastic Materials by Multiphysical Nondestructive Methods: A Review. *Applied Sciences*, 10(5). <https://doi.org/10.3390/app10051588>

Huang, Y.-C., Chang, S.-Y., & Chang, C.-H. (2009). Effect of residual stresses on mechanical properties and interface adhesion strength of SiN thin films. *Thin Solid Films*, 517(17), 4857-4861. <https://doi.org/10.1016/j.tsf.2009.03.043>

Hussein, A., Hao, L., Yan, C., & Everson, R. (2013). Finite element simulation of the temperature and stress fields in single layers built without-support in selective laser melting. *Materials & Design* (1980-2015), 52, 638-647. <https://doi.org/10.1016/j.matdes.2013.05.070>

Hwang, Seulgi, Won-Jung Oh, Dong-Hyun Kim, Jung Gi Kim, Jeong Seok Oh, Tae-Hyun Nam, Chung-Soo Kim, and Taekyung Lee. 2023. "Optimizing interlayer cooling for SUS316L thin wall fabricated by directed energy deposition." *Journal of Materials Research and Technology* 23: 5239-5245. <https://doi.org/10.1016/j.jmrt.2023.02.145>.

Hwa, Yoon, Christopher S. Kumai, Thomas M. Devine, Nancy Yang, Joshua K. Yee, Ryan Hardwick, and Kai Burgmann. 2021. "Microstructural banding of directed energy deposition-additively manufactured 316L stainless steel." *Journal of Materials Science & Technology* 69: 96-105. <https://doi.org/10.1016/j.jmst.2020.08.022>.

Hensley, C., Sisco, K., Beauchamp, S., Godfrey, A., Rezayat, H., McFalls, T., Galicki, D., List, F., Carver, K., Stover, C., Gandy, D. W., & Babu, S. S. (2021). Qualification pathways for

additively manufactured components for nuclear applications. *Journal of Nuclear Materials*, 548. <https://doi.org/10.1016/j.jnucmat.2021.152846>

Izadi, Mojtaba, Aidin Farzaneh, Ian Gibson, and Bernard F. Rolfe. 2017. "The effect of process parameters and mechanical properties of direct energy deposited stainless steel 316."

Jackson, J. (2024, 03 07). Retrieved from Gain.inl.gov: https://gain.inl.gov/content/uploads/4/2024/05/01-DOE_MicroreactorProgramAndMARVEL2024.pdf

Kartikeya Sarma, I., V. Srinivas, and S. Kanmani Subbu. 2021. "Effect of process parameters on micro hardness, bulk hardness and porosity of LENSTM deposited SS 316L alloy." *Materials Today: Proceedings* 46: 2616-2624. <https://doi.org/10.1016/j.matpr.2021.02.268>.

Kim, Choong S. 1975. *Thermophysical Properties of Stainless Steels*. Argonne National Laboratory ANL-75-55, Argonne National Laboratory, Argonne, Illinois.

Kumaran, M., V. Senthilkumar, C. T. Justus Panicker, and R. Shishir. 2021. "Investigating the residual stress in additive manufacturing of combined process in powder bed fusion and directed energy deposition." *Materials Today: Proceedings* 47: 4387-4390. <https://doi.org/10.1016/j.matpr.2021.05.200>.

Laboratory, I. N. (2022). *Microreactor Applications Research Validation and Evaluation Project (MARVEL)*. Retrieved from https://factsheets.inl.gov/FactSheets/20-50248_MARVEL_Fact_Sheet_R15.pdf

Lee, Y., Feldhausen, T., Fancher, C. M., Nandwana, P., Babu, S. S., Simunovic, S., & Love, L. J. (2024). Prediction of residual strain/stress validated with neutron diffraction method for wire-feed hybrid additive/subtractive manufacturing. *Additive Manufacturing*, 79. <https://doi.org/10.1016/j.addma.2023.103920>

Li, M., D. Andersson, R. Dehoff, A. Jokisaari, I. Van Rooyen, and D. Cairns-Gallimore, 2022. *Advanced Materials and Manufacturing Technologies (AMMT) 2022 Roadmap*, ANL-23/12

Lin, Pei-Yi, Fang-Cheng Shen, Kuo-Tsai Wu, Sheng-Jye Hwang, and Huei-Huang Lee. 2020. "Process optimization for directed energy deposition of SS316L components." *The International Journal of Advanced Manufacturing Technology* 111 (5-6): 1387-1400. <https://doi.org/10.1007/s00170-020-06113-z>.

Lister, F., R. Dehoff, K. Carver, C. Joslin, B. Jordan, R. Duncan, J. R. Matheson. 2024. "Fabrication of a liner assembly for the marvel microreactor, ORNL/TM-2024/3332

Liu, Y., Yang, Y., & Wang, D. (2016). A study on the residual stress during selective laser melting (SLM) of metallic powder. *The International Journal of Advanced Manufacturing Technology*, 87(1-4), 647-656. <https://doi.org/10.1007/s00170-016-8466-y>

Lu, X., Chiumenti, M., Cervera, M., Li, J., Lin, X., Ma, L., Zhang, G., & Liang, E. (2021). Substrate design to minimize residual stresses in Directed Energy Deposition AM processes. *Materials & Design*, 202. <https://doi.org/10.1016/j.matdes.2021.109525>,

Majumdar, J. Dutta, A. Pinkerton, Z. Liu, I. Manna, and L. Li. 2005. "Microstructure characterisation and process optimization of laser assisted rapid fabrication of 316L stainless steel." *Applied Surface Science* 247 (1-4): 320-327.
<https://doi.org/10.1016/j.apsusc.2005.01.039>.

MDC Precision. "90 deg elbow, 6" Flange, long" (2023). <https://www.mdcprecision.com/90-deg-elbow-6-flange-long>

Measurement of Residual Stress in Materials Using Neutrons. (2005). INTERNATIONAL ATOMIC ENERGY AGENCY. <https://www.iaea.org/publications/7215/measurement-of-residual-stress-in-materials-using-neutrons>

Mercelis, P., & Kruth, J. P. (2006). Residual stresses in selective laser sintering and selective laser melting. *Rapid Prototyping Journal*, 12(5), 254-265.
<https://doi.org/10.1108/13552540610707013>

Mithal, A., Maharjan, N., Tan, N. Y. J., Chew, Y., & Idapalapati, S. (2024). Understanding residual stress evolution in directed energy deposition with interlayer deformation. *Journal of Manufacturing Science and Engineering*, 1-25. <https://doi.org/10.1115/1.4066333>

Moon, J. H., Baek, S. M., Lee, S. G., Seong, Y., Amanov, A., Lee, S., & Kim, H. S. (2018). Effects of residual stress on the mechanical properties of copper processed using ultrasonic-nanocrystalline surface modification. *Materials Research Letters*, 7(3), 97-102.
<https://doi.org/10.1080/21663831.2018.1560370>

Mugwagwa, L., Dimitrov, D., Matope, S., & Yadroitsev, I. (2018). Influence of process parameters on residual stress related distortions in selective laser melting. *Procedia Manufacturing*, 21, 92-99. <https://doi.org/https://doi.org/10.1016/j.promfg.2018.02.099>

Mugwagwa, L., Yadroitsava, I., Makoana, N. W., & Yadroitsev, I. (2021). Residual stress in laser powder bed fusion. In *Fundamentals of Laser Powder Bed Fusion of Metals* (pp. 245-276). <https://doi.org/10.1016/b978-0-12-824090-8.00014-7>

Nelson, A. T. (2023). Prospects for additive manufacturing of nuclear fuel forms. *Progress in Nuclear Energy*, 155. <https://doi.org/10.1016/j.pnucene.2022.104493>

Nickel Institute. 2020. High-Temperature Characteristics of Stainless Steels; Available from: https://nickelinstitute.org/media/4657/ni_aisi_9004_hightemperaturecharacteristics.pdf

Noyan, I. C., Huang, T. C., & York, B. R. (1995). Residual stress/strain analysis in thin films by X-ray diffraction. *Critical Reviews in Solid State and Materials Sciences*, 20(2), 125-177.
<https://doi.org/10.1080/10408439508243733>

Orye, Davy. "Additive Manufacturing of Support-Free Shrouded Impellers." LinkedIn, November 16, 2021. <https://www.linkedin.com/pulse/additive-manufacturing-support-free-shrouded-impellers-davy-orye/>

Pacheco, J. T., Meura, V. H., Bloemer, P. R. A., Veiga, M. T., de Moura Filho, O. C., Cunha, A., & Teixeira, M. F. (2022). Laser directed energy deposition of AISI 316L stainless steel: The effect of build direction on mechanical properties in as-built and heat-treated conditions.

Advances in Industrial and Manufacturing Engineering, 4.
<https://doi.org/10.1016/j.aime.2022.100079>

Phan, T. Q., Strantz, M., Hill, M. R., Gnaupel-Herold, T. H., Heigel, J., D'Elia, C. R., DeWald, A. T., Clausen, B., Pagan, D. C., Peter Ko, J. Y., Brown, D. W., & Levine, L. E. (2019). Elastic Residual Strain and Stress Measurements and Corresponding Part Deflections of 3D Additive Manufacturing Builds of IN625 AM-Bench Artifacts Using Neutron Diffraction, Synchrotron X-Ray Diffraction, and Contour Method. Integrating Materials and Manufacturing Innovation, 8(3), 318-334. <https://doi.org/10.1007/s40192-019-00149-0>

Piscopo, G., Salmi, A., & Atzeni, E. (2021). Influence of High-Productivity Process Parameters on the Surface Quality and Residual Stress State of AISI 316L Components Produced by Directed Energy Deposition. Journal of Materials Engineering and Performance, 30(9), 6691-6702. <https://doi.org/10.1007/s11665-021-05954-3>

Piscopo, Gabriele, and Luca Iuliano. 2024. "Evaluating the Effect of Deposition Strategy on Mechanical Characteristics of 316L Parts Produced by Laser Powder Directed Energy Deposition Process." Lasers in Manufacturing and Materials Processing 11 (2): 419-436. <https://doi.org/10.1007/s40516-024-00251-y>.

Polyzos, E., Pulju, H., Mackel, P., Hinderdael, M., Ertveldt, J., Van Hemelrijck, D., & Pyl, L. (2023). Measuring and Predicting the Effects of Residual Stresses from Full-Field Data in Laser-Directed Energy Deposition. Materials (Basel), 16(4). <https://doi.org/10.3390/ma16041444>

Prime, M. B. (2000). Cross-Sectional Mapping of Residual Stresses by Measuring the Surface Contour After a Cut. Journal of Engineering Materials and Technology, 123(2), 162-168. <https://doi.org/10.1115/1.1345526>

Roehling, J. D., Smith, W. L., Roehling, T. T., Vrancken, B., Guss, G. M., McKeown, J. T., Hill, M. R., & Matthews, M. J. (2019). Reducing residual stress by selective large-area diode surface heating during laser powder bed fusion additive manufacturing. Additive Manufacturing, 28, 228-235. <https://doi.org/10.1016/j.addma.2019.05.009>

Romano, S., Brückner-Foit, A., Brandão, A., Gumpinger, J., Ghidini, T., & Beretta, S. (2018). Fatigue properties of AISi10Mg obtained by additive manufacturing: Defect-based modelling and prediction of fatigue strength. Engineering Fracture Mechanics, 187, 165-189. <https://doi.org/10.1016/j.engfracmech.2017.11.002>

Rossini, N. S., Dassisti, M., Benyounis, K. Y., & Olabi, A. G. (2012). Methods of measuring residual stresses in components. Materials & Design, 35, 572-588. <https://doi.org/10.1016/j.matdes.2011.08.022>

Salmi, Alessandro, Gabriele Piscopo, Adriano Nicola Pilagatti, and Eleonora Atzeni. 2024. "Evaluation of Porosity in AISI 316L Samples Processed by Laser Powder Directed Energy Deposition." Journal of Manufacturing and Materials Processing 8 (4). <https://doi.org/10.3390/jmmp8040129>.

Sandmeyer Steel Company. 2014. Specification Sheet: Alloy 316/316L; Available from: <https://www.sandmeyersteel.com/images/316-316L-317L-Spec-Sheet.pdf>

- Sciammarella, Federico M., and Benyamin Salehi Najafabadi. 2018. "Processing Parameter DOE for 316L Using Directed Energy Deposition." *Journal of Manufacturing and Materials Processing* 2 (3). <https://doi.org/10.3390/jmmp2030061>.
- Schröder, J., Evans, A., Mishurova, T., Ulbricht, A., Sprengel, M., Serrano-Munoz, I., Fritsch, T., Kromm, A., Kannengießer, T., & Bruno, G. (2021). Diffraction-Based Residual Stress Characterization in Laser Additive Manufacturing of Metals. *Metals*, 11(11). <https://doi.org/10.3390/met11111830>
- Simson, T., Emmel, A., Dwars, A., & Böhm, J. (2017). Residual stress measurements on AISI 316L samples manufactured by selective laser melting. *Additive Manufacturing*, 17, 183-189. <https://doi.org/10.1016/j.addma.2017.07.007>
- Strantz, M., Vrancken, B., Prime, M. B., Truman, C. E., Rombouts, M., Brown, D. W., Guillaume, P., & Van Hemelrijck, D. (2019). Directional and oscillating residual stress on the mesoscale in additively manufactured Ti-6Al-4V. *Acta Materialia*, 168, 299-308. <https://doi.org/10.1016/j.actamat.2019.01.050>
- Svetlizky, David, Mitun Das, Baolong Zheng, Alexandra L. Vyatskikh, Susmita Bose, Amit Bandyopadhyay, Julie M. Schoenung, Enrique J. Lavernia, and Noam Eliaz. 2021. "Directed energy deposition (DED) additive manufacturing: Physical characteristics, defects, challenges and applications." *Materials Today* 49: 271-295. <https://doi.org/10.1016/j.mattod.2021.03.020>.
- Van Rooyen, I. J., 2024. "GIF AMME Working Group", IAEA Technical Meeting on the Deployment of Advanced Manufacturing Solutions for the Nuclear Power Industry, 19-22 August 2024
- Voisin, T., Forien, J.-B., Perron, A., Aubry, S., Bertin, N., Samanta, A., Baker, A., & Wang, Y. M. (2021). New insights on cellular structures strengthening mechanisms and thermal stability of an austenitic stainless steel fabricated by laser powder-bed-fusion. *Acta Materialia*, 203. <https://doi.org/10.1016/j.actamat.2020.11.018>
- Wei, H. L., Mukherjee, T., Zhang, W., Zuback, J. S., Knapp, G. L., De, A., & DebRoy, T. (2021). Mechanistic models for additive manufacturing of metallic components. *Progress in Materials Science*, 116. <https://doi.org/10.1016/j.pmatsci.2020.100703>
- Wilkinson, A. J., & Britton, T. B. (2012). Strains, planes, and EBSD in materials science. *Materials Today*, 15(9), 366-376. [https://doi.org/10.1016/s1369-7021\(12\)70163-3](https://doi.org/10.1016/s1369-7021(12)70163-3)
- Wilkinson, A. J., Meaden, G., & Dingley, D. J. (2006). High-resolution elastic strain measurement from electron backscatter diffraction patterns: new levels of sensitivity. *Ultramicroscopy*, 106(4-5), 307-313. <https://doi.org/10.1016/j.ultramic.2005.10.001>
- Woo, W., An, G. B., Kingston, E. J., DeWald, A. T., Smith, D. J., & Hill, M. R. (2013). Through-thickness distributions of residual stresses in two extreme heat-input thick welds: A neutron diffraction, contour method and deep hole drilling study. *Acta Materialia*, 61(10), 3564-3574. <https://doi.org/10.1016/j.actamat.2013.02.034>
- Wright, S. I., Nowell, M. M., & Field, D. P. (2011). A review of strain analysis using electron backscatter diffraction. *Microsc Microanal*, 17(3), 316-329. <https://doi.org/10.1017/S1431927611000055>

Wu, A. S., Brown, D. W., Kumar, M., Gallegos, G. F., & King, W. E. (2014). An Experimental Investigation into Additive Manufacturing-Induced Residual Stresses in 316L Stainless Steel. *Metallurgical and Materials Transactions A*, 45(13), 6260-6270. <https://doi.org/10.1007/s11661-014-2549-x>

Yadollahi, Aref, Nima Shamsaei, Youssef Hammi, and Mark F. Horstemeyer. 2016. "Quantification of tensile damage evolution in additive manufactured austenitic stainless steels." *Materials Science and Engineering: A* 657: 399-405. <https://doi.org/10.1016/j.msea.2016.01.067>.

Yadollahi, Aref, Nima Shamsaei, Scott M. Thompson, and Denver W. Seely. 2015. "Effects of process time interval and heat treatment on the mechanical and microstructural properties of direct laser deposited 316L stainless steel." *Materials Science and Engineering: A* 644: 171-183. <https://doi.org/10.1016/j.msea.2015.07.056>.

Yatomi, M., A. D. Bettinson, N. P. O'Dowd, and K. M. Nikbin. 2004. "Modelling of damage development and failure in notched-bar multiaxial creep tests." *Fatigue & Fracture of Engineering Materials & Structures* 27 (4): 283-295. <https://doi.org/10.1111/j.1460-2695.2004.00755.x>.

Yadroitsev, I., & Yadroitsava, I. (2015). Evaluation of residual stress in stainless steel 316L and Ti6Al4V samples produced by selective laser melting. *Virtual and Physical Prototyping*, 10(2), 67-76. <https://doi.org/10.1080/17452759.2015.1026045>

Zhang, X., McMurtrey, M. D., Wang, L., O'Brien, R. C., Shiau, C.-H., Wang, Y., Scott, R., Ren, Y., & Sun, C. (2020). Evolution of Microstructure, Residual Stress, and Tensile Properties of Additively Manufactured Stainless Steel Under Heat Treatments. 72. <https://doi.org/10.1007/s11837-020-04433-9>. *JOM. Journal of the Minerals, Metals & Materials Society*; Journal Volume: 72; Journal Issue: 12

Zhong, Y., Rännar, L.-E., Liu, L., Koptug, A., Wikman, S., Olsen, J., Cui, D., & Shen, Z. (2017). Additive manufacturing of 316L stainless steel by electron beam melting for nuclear fusion applications. *Journal of Nuclear Materials*, 486, 234-245. <https://doi.org/10.1016/j.jnucmat.2016.12.042>

Zhang, W., Guo, D., Wang, L., Davies, C. M., Mirihanage, W., Tong, M., & Harrison, N. M. (2023). X-ray diffraction measurements and computational prediction of residual stress mitigation scanning strategies in powder bed fusion additive manufacturing. *Additive Manufacturing*, 61. <https://doi.org/10.1016/j.addma.2022.103275>

Zhou, C., Wang, J., Hu, S., Tao, H., Fang, B., Li, L., Zheng, J., & Zhang, L. (2020). Enhanced Corrosion Resistance of Additively Manufactured 316L Stainless Steel After Heat Treatment. *Journal of The Electrochemical Society*, 167(14). <https://doi.org/10.1149/1945-7111/abc10e>

Pacific Northwest National Laboratory

902 Battelle Boulevard
P.O. Box 999
Richland, WA 99354

1-888-375-PNNL (7665)

www.pnnl.gov